MarchenkovAY@mpei.ru

STRUCTURAL-PHASE TRANSFORMATIONS IN HIGH-ALLOYED STEELS UNDER VARIOUS TYPES OF LOADING

Matyunin V.M., Marchenkov A.Yu., Zhgut D.A., Agafonov R.Yu., Pankina A.A.
Moscow Power Engineering Institute

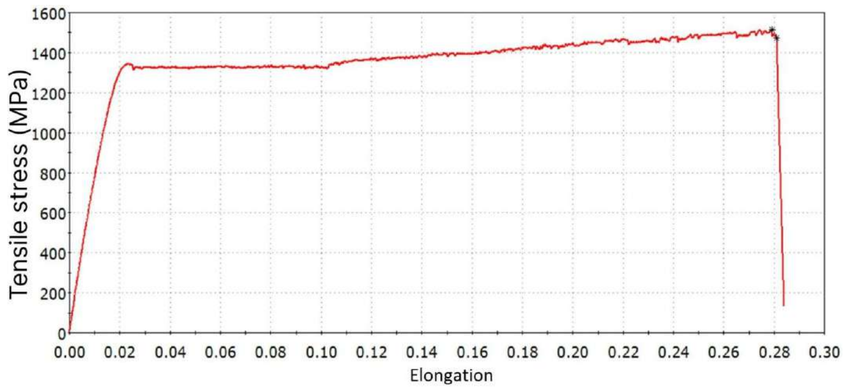

Tensile stress diagram of 23Kh15N5AM3Sh steel (dual-phase structure, Austenite + martensite)

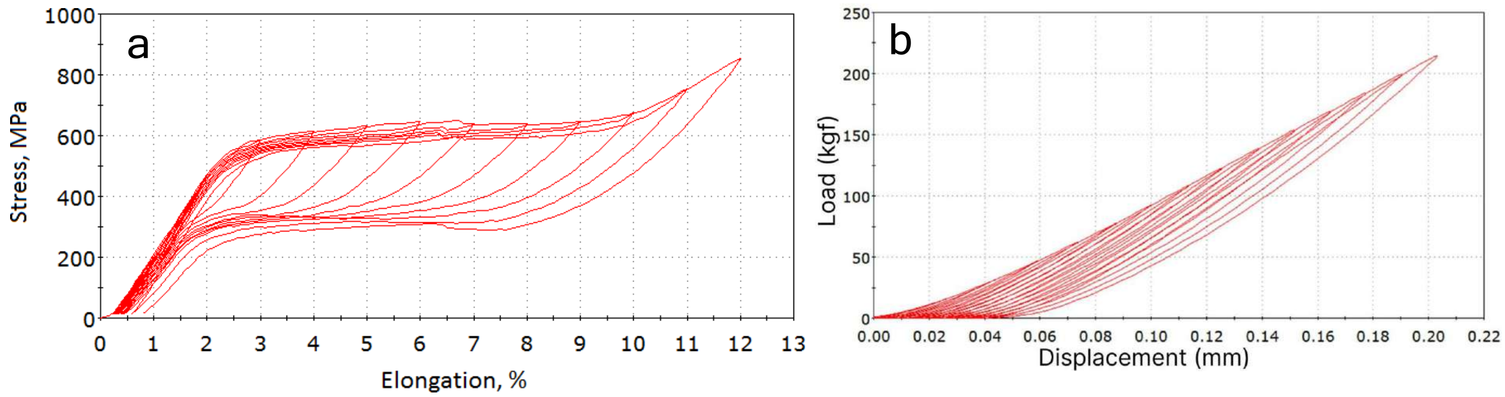

Superelasticity in titanium nickelide alloys (reversible austenitic-martensite transformation during tension (a) and indentation (b))

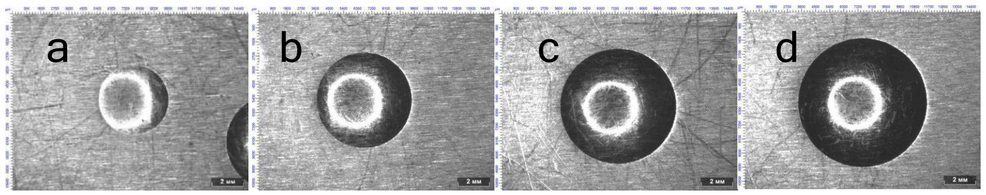

Indents on DI-59 steel (10Kh13G12N2S2D2B) at various indentation load

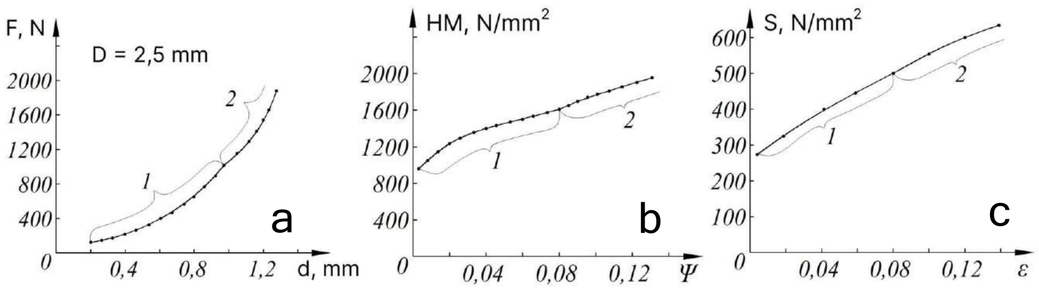

Step indentation diagram (a), “Meyer hardness HM – indentation strain Ψ” dependence (b) and “True stress S – true tension strain ε” dependence (c) for DI-59 steel

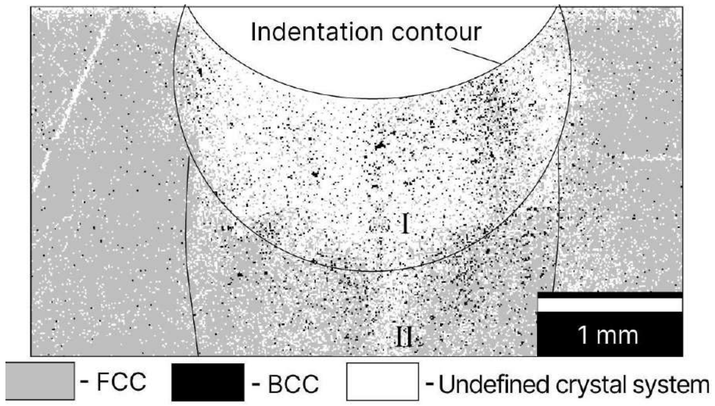

The results of determining the crystal lattice type in the metal under the indent a ball indenter on steel DI59 (scanning electron microscopy)

Original austenite structure

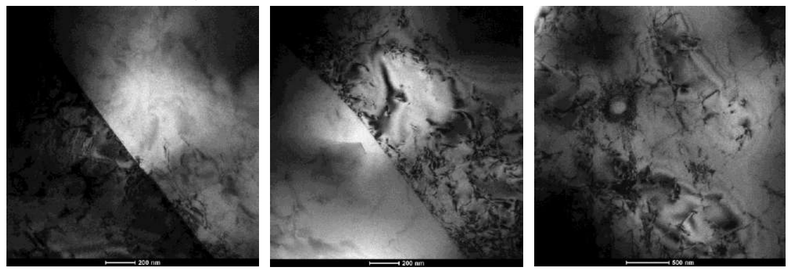

Deformed metal structure (martensite)

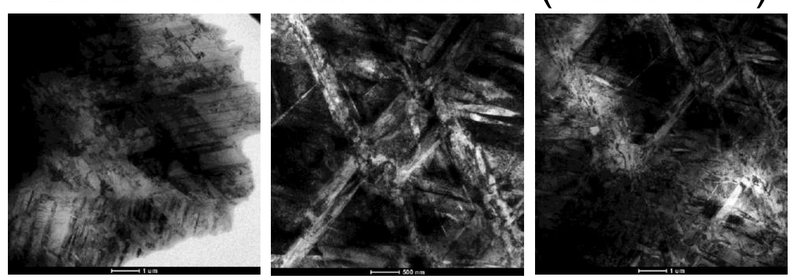

Microstructure of metal under the indent on steel DI59 (transmission electron microscopy)

IV International Conference and School "Advanced High Entropy Materials"
September 26-30, 2022

№36

mikheev@bmstu.ru

ORGANIZATION OF FUNCTIONAL LAYERS OF COMPOSITE COATINGS FOR TRIBOTECHNICAL APPLICATION

Mikheev R.S.[1*], Kalashnikov I.E.[2], Kobeleva L.I.[2], Bykov P.A.[2]

[1] Bauman Moscow State Technical University; [2] Baikov Institute of Metallurgy and Materials Science RAS

Introduction: Expansion of the plain bearings application areas can be achieved by organization of functional layers of composite coatings for tribotechnical application. Such materials should consist of a steel base that perceives the load, intermediate technological layers that provide the required adhesive strength, as well as layers formed directly during the synthesis of the composition and layers with a composite structure that have the required level of tribotechnical properties.

Scheme of functional layers of composite coatings organization:

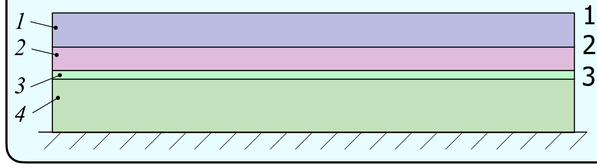

1: working layer, wt.% - Al-12Si + 10 $SiC_{(40)}$
2: intermediate technological layer - AD1 (GOST 4784)
3: intermetallic layer (formed directly during the composition synthesis) - Al_xFe_y
4: substrate - steel 20 (GOST 1050)

Intermediate technological layer formation by explosion welding process[1)]:

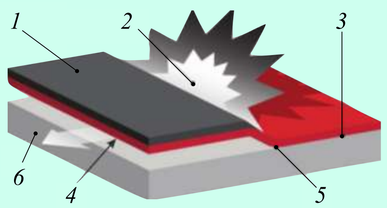

1: explosive substance - ammonite №6GB (GOST 21984)
2: detonation front
3: intermetallic layer
4: intermediate technological layer
5: collision point
6: substrate
welding speed - (2000-2200) m/s;
collision speed - 380 m/s

[1)] was carried out in VSTU by Prof. S.V. Kuzmin

Working layer formation by argon arc surfacing process:

1: working layer
2: intermediate technological layer
3: intermetallic layer
4: substrate
5: filler composite rod, wt.%:
Al-12Si + 10 $SiC_{(40)}$
(rod's size according GOST 21449:
Ø 5±0,1 mm; L=450 ± 9 mm)

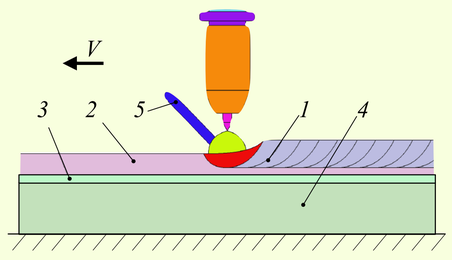

current (I): 120-160 A; surfacing speed (V): 11-13 m/h
arc voltage (U): 18-20 V; argon consumption (V_{Ar}): 12-15 l/min

Friction and wear tests of composite coatings:

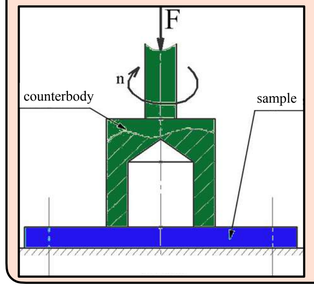

axial load (F), N	18 - 215
pressure (p), MPa	0,2 - 2,56
rotation frequency (n), rpm	540
speed (V), m/s	0,39
work tension (pV), MPa m/s	0,08 - 1,0
test duration (t), s	600
counterbody	steel (HRC≥45)

Microstructure of composite coatings:

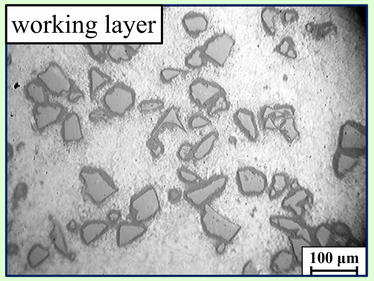

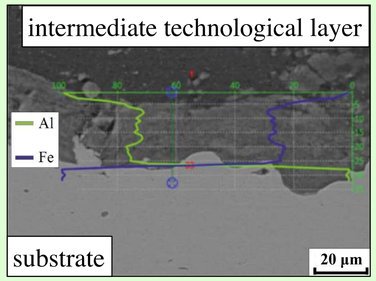

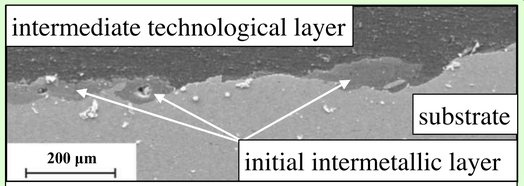

h_m=16 µm (h_{min}=5 µm; h_{max}=30 µm)

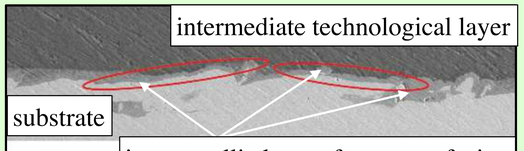

h_m=16 µm (h_{min}=6 µm; h_{max}=30 µm)

Tribotechnical properties of composite coatings:

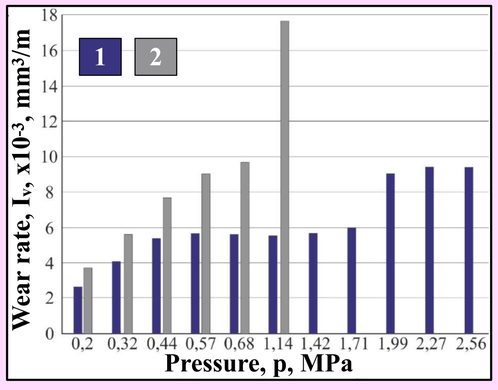

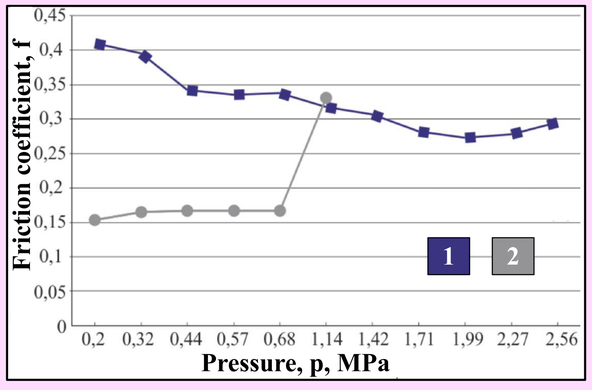

Working layer composition, wt.%: 1: Al-12Si + 10 $SiC_{(40)}$ 2: B83[2)] (GOST 1320)

[2)] industrial bimetallic sample made of steel 20 (GOST 1050) coated with B83 grade babbit alloy.

Samples surface after friction and wear tests:

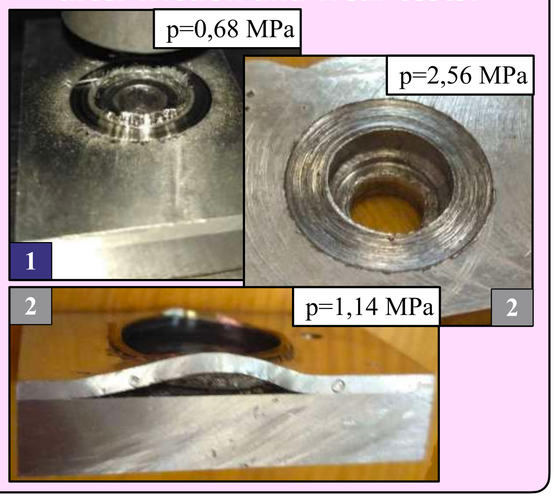

Conclusions:

New layered composite materials have been manufactured using explosion welding and argon arc surfacing processes. They are a steel base (steel 20 GOST 1050), an intermediate technological layer (aluminum AD1 GOST 4784), an intermetallic layer (Al_xFe_y system) and a working layer (composite material Al-12Si + 10 wt.% $SiC_{(40)}$).

Friction and wear test results showed that the use of manufactured samples in sliding friction units will expand the range of triboloading, as well as reduce wear rate by up to 50% compared to bimetallic materials made of steel 20 coated with B83 babbitt.

Acknowledgements. This research was supported by a grant from the Russian Science Foundation (project No. 22-29-00366).

IV International Conference and School "Advanced High Entropy Materials"
September 26-30, 2022

№37

NaumovStanislav@yandex.ru

Naumov S.V., Panov D.O., Chernichenko R.S., Stepanov N.D., Zherebtsov S.V., Neulybin S.D., Salishchev G.A.

WELDING TECHNIQUES OF Ti_2AlNb BASED ALLOYS

Nowadays, plasma, laser, diffusion, and electric resistance welding of Ti_2AlNb-based alloys attract greatest interest. Various techniques for welding of such alloys are considered and proposed in the work. A defect-free weld with an optimal structure is formed due to the high welding speed and the concentration of thermal energy or the absence of the need to melt the metal. The welding modes are selected and the technological features of plasma, laser, diffusion, and electric resistance welding with obtaining the optimal structural state and strength properties up to 90% of the base metal.

Laser Welding Technology

Laser beam welding

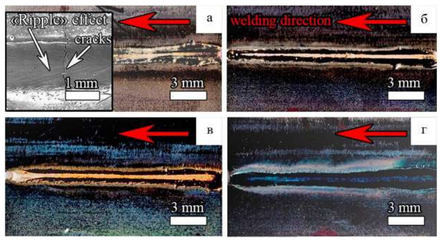

Figure - 1. Appearance of welds obtained at: a) room temperature; b) preheating 400 °C; c) 600 °C; d) 800 °C. The red arrows indicate the direction of the laser beam welding.

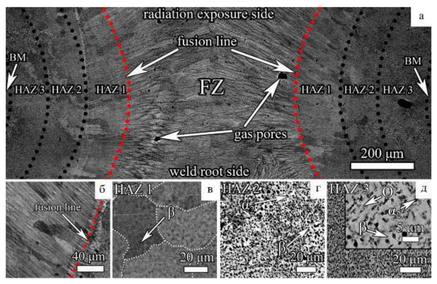

Figure - 2. Transverse structure of the weld after LBW at room temperature: a) macrostructure; b) FZ; c) HAZ1; d) HAZ2 e) HAZ3.

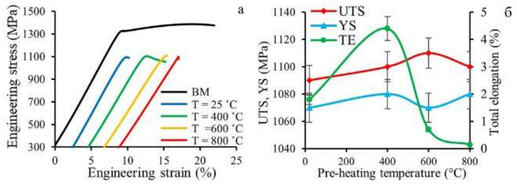

Figure - 3. Mechanical properties of welded joints obtained by LBW: a) stress-strain curves of the initial state and welded joints; b) dependence of properties on preheating temperature.

Pulsed laser beam welding

Figure - 4. Equipment for laser welding of the LAT-S-300 series.

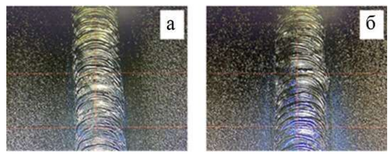

Figure - 5. Appearance of the welded joint depending on the voltage and pulse duration: a) 280 V, 6 ms; b) 300 V, 6 ms.

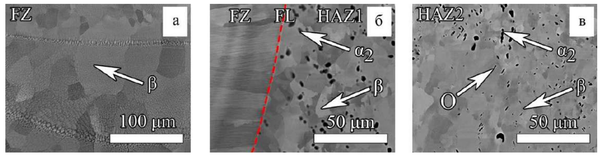

Figure - 6. Zones of the Ti_2AlNb welded joint obtained by PLBW at 300 V, 6 ms modes: a) melting zone (FZ); b) fusion line (FL) and first heat affected zone (HAZ1); c) second heat affected zone (HAZ2).

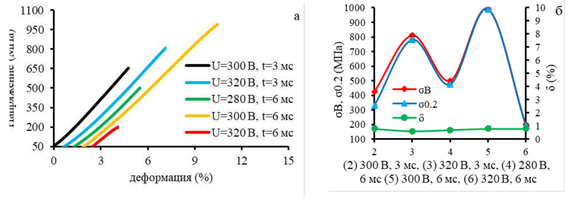

Figure - 7. Mechanical properties of welded joints: a) tensile diagram; b) graph of the mechanical properties of the welded joint depending on the modes of PLBW.

Electron Beam Welding

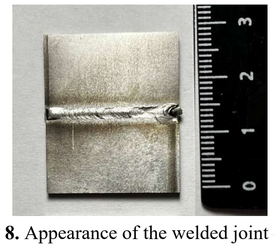

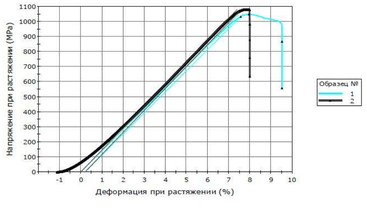

Figure - 8. Appearance of the welded joint obtained by EBW and tensile graph of welded joints.

Plasma Welding Technology

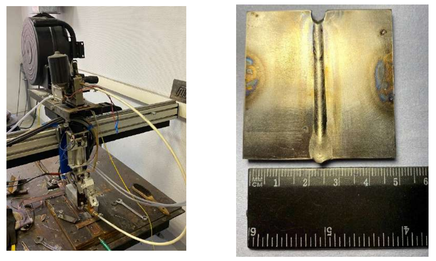

Figure - 9. Plasma welding equipment and the appearance of the welded joint.

TIG welding

Figure - 10. TIG-welding equipment.

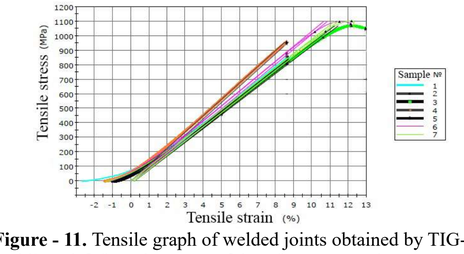

Figure - 11. Tensile graph of welded joints obtained by TIG-welding: 1-2 forced currents; 3 low frequency pulse current; 4-7 high frequency pulse current

Diffusion welding technology

VTI-4 alloy was used in this work (Ti-23Al-23Nb-1.4V-0.8Zr-0.4Mo-0.4Si at. %). DW was carried out on SPS 10–3 spark plasma sintering unit (Fig. 12). The templets were heated by passing pulsed currents through stamping punch and graphite matrix (Fig. 13). The blank deformation rate was no more than 10 %. Mechanical behavior of the templets was evaluated using tensile deformation. Enhanced mechanical properties were observed after welding temperature of 940 °C and 960 °C, equalizing time of 2 hours and pressure of 16–18 Mpa (Fig. 16). With an increase in the welding temperature, O-phase content in blanks increases but α_2-phase content remains almost unchanged. However, with respect to the base material there is a drastic increase in the O-phase (Fig. 15).

Diffusion welding

Figure - 12. Equipment SPS 10-3 for diffusion welding in vacuum (10^{-4} Torr).

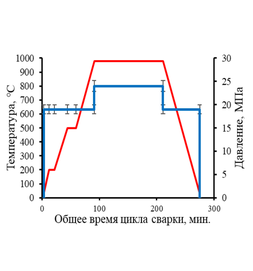

Figure - 13. Welding cyclogram and image of the placement of samples inside the matrix with punches: 1 - upper punch; 2 - corundum electrically insulating plate; 3 - matrix; 4 - welded samples; 5 lower punch with a technological hole for a thermocouple.

Electric resistance welding

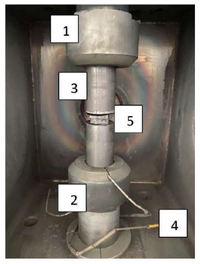

Figure - 14. Scheme of placement of blanks before electric resistance welding: 1 - hydraulic cylinder, 2 - graphite insert, 3 - punches, 4 - thermocouple, 5 - welded blanks.

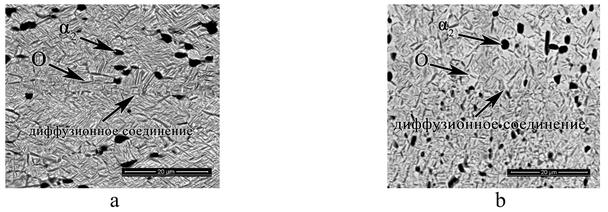

Figure - 15. Microstructure of the diffusion bonding of an alloy based on Ti_2AlNb, x5000: a) diffusion welding; b) electric resistance welding.

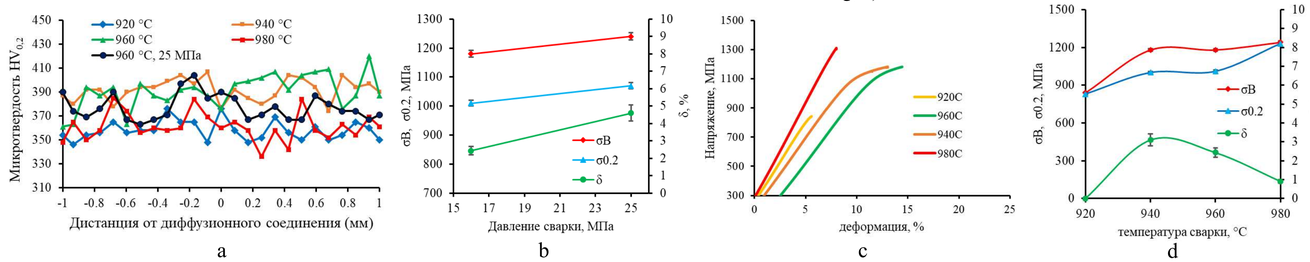

Figure - 16. Mechanical properties of diffusion joints: a) microhardness of the diffusion joints; b), c) graphs of the mechanical properties of diffusion joints depending on the welding temperature; d) mechanical properties of the diffusion joint at a temperature of 960 °C depending on the welding pressure.

The authors gratefully acknowledge the financial support from the Russian Science Foundation Grant № 19-79-30066. The authors are grateful to the personnel of the Joint Research Center, «Technology and Materials», Belgorod State National Research University, for their assistance with the instrumental analysis.

IV International Conference and School "Advanced High Entropy Materials"
September 26-30, 2022

№ 39

STUDY OF ALMG6+TITANIUM WELD INTERFACE AFTER EXPLOSIVE WELDING

nemat199595@mail.ru

Niyozbekov N. N[1]., Saikov I. V[1]., Mironov S. Yu[2]., Kaibyshev R. O[2].,Dolzhenko P. D[2]. Malakhov A. Yu[1]., Denisov I. V[1].

[1]Merzhanov Institute of Structural Macrokinetics and Materials Science Russian Academy of Sciences, Chernogolovka, Russia

[2]Belgorod State University, Belgorod, Russia

Introduction

Composite materials based on aluminum alloys and titanium, due to the combination of high specific strength and corrosion resistance are widely used in aircraft building, shipbuilding, petrochemical engineering, etc. Aluminum alloys and titanium have a significant difference in physical and mechanical properties. Therefore, the brittle intermetallic phases TixAly are formed at the weld interface, which reduce the mechanical properties of composite materials [1]. In view of the fact, explosive welding (as solid state welding method) is widely used to produce the composite materials consisting of aluminum alloys and titanium.

The aim of the study was to examine in detail the microstructure of the weld interface and the mechanical properties of AlMg6 + titanium composite material produced by explosive welding.

Materials and methods

In the experiment, commercially available plates of AlMg6 and titanium were used. The explosive used in the experiment is a mixture of microporous ammonium nitrate and diesel oil (ANFO). The detonation velocity was about 2500 m/s. The setup of the experiments is shown in Figure 1.

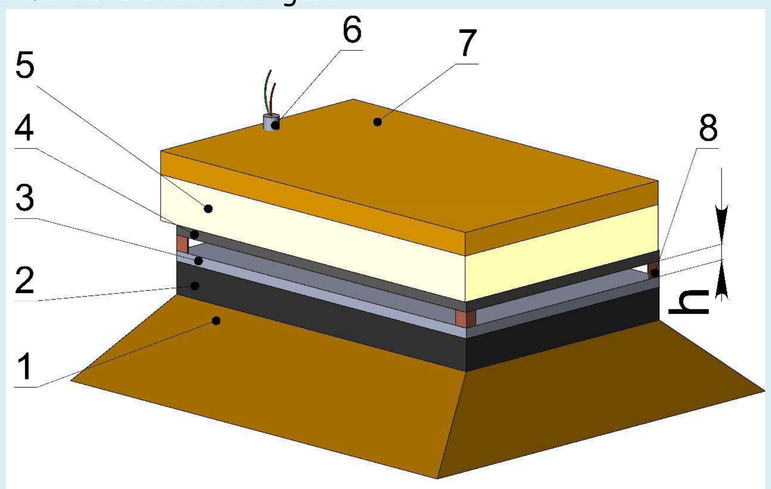

Figure 1. Basic setup for explosive welding : 1 —sand support; 2—anvil; 3—parent plate (Titanium); 4—flyer plate (AlMg6); 5—explosive; 6—detonator; 7 — sand stemming; 8—support; h - stand off distance.

As a result, the composite material AlMg6+titanium with a size of (4+5)×200×300 mm was produced.

Results

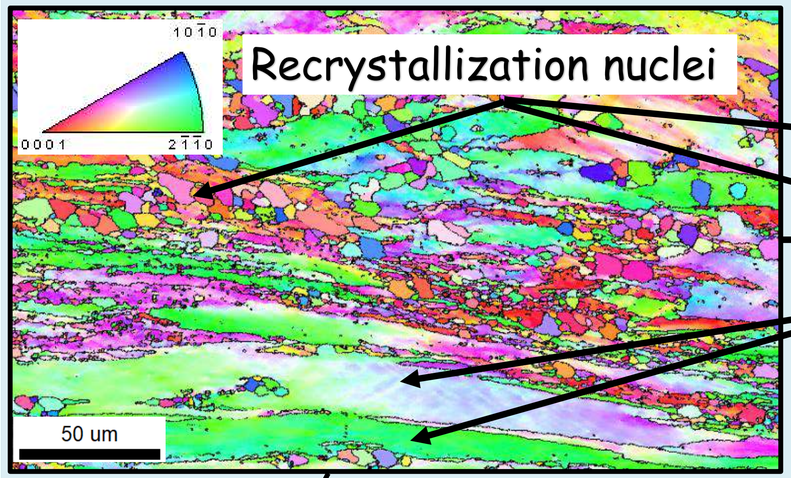

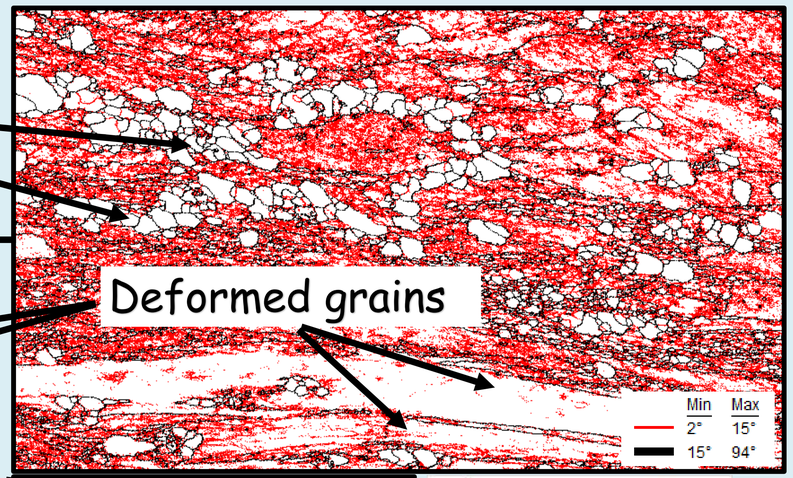

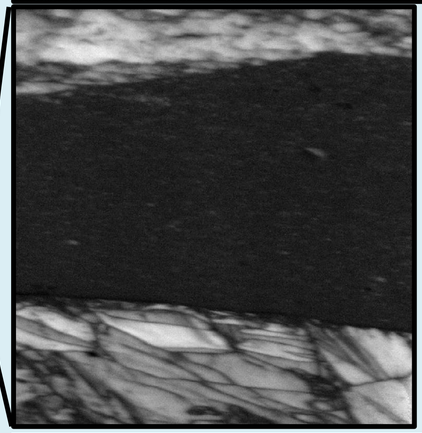

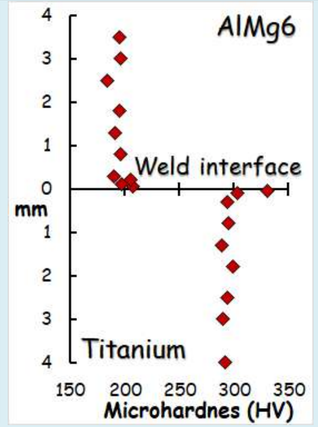

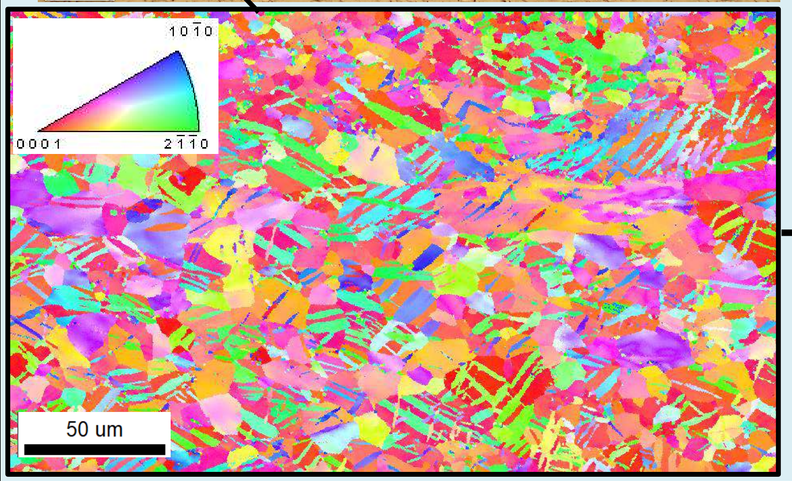

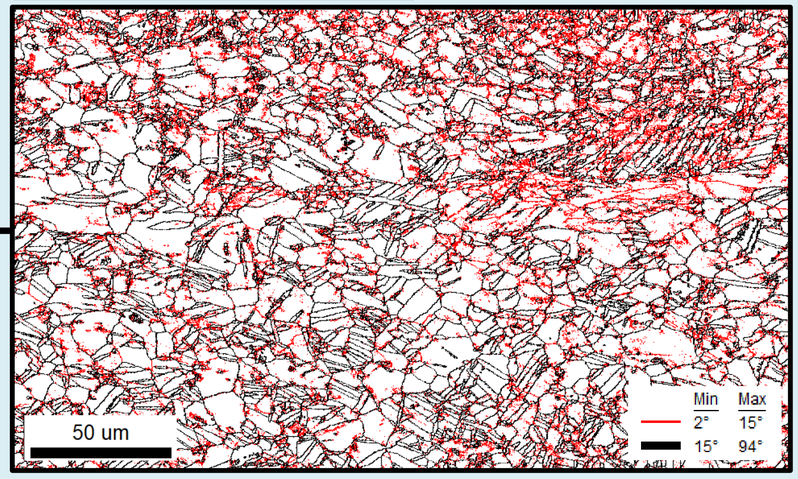

This research was performed by using the set of modern scientific instruments available for multiple accesses at the ISMAN Center of Shared Services and the Center for Collective Use "Technologies and Materials of the National Research University BelSU "

IV International Conference and School "Advanced High Entropy Materials"
September 26-30, 2022

№ 40

E-mail: alena_novoselova@list.ru

ELECTROCHEMICAL FORMATION OF Ln-Ga-Al AND Ln-Ga-In (Ln = La, Pr, Dy) ALLOYS IN LIQUID METAL / MOLTEN SALT SYSTEM. THERMODYNAMICS OF TRIPLE COMPOUNDS

A.V. Novoselova and V.V. Smolenski

Institute of High-Temperature Electrochemistry UB RAS, Ekaterinburg, 620990, Russia

Introduction

Nuclear power, as a kind of "green and clean" energy, is currently considered as a promising candidate for the future because of its enormous efficiency, cost-effectiveness and lack of greenhouse gas generation. A limiting factor in its development is the lack of modern technology for the disposal of spent nuclear fuel and high-level nuclear waste. Currently, research is underway for creation a closed nuclear cycle with using molten salts. It is known that lanthanides are neutron poisons, and therefore they must be separated and concentrated from the basic components of the fuel during its reprocessing. Therefore, these investigations are aimed for studying the electrochemical processes of the alloys formation and determining principal thermodynamic characteristics of triple compounds in "liquid metal-molten salt" system.

For calculation of the principal thermodynamic characteristics of the alloy formation processes open-circuit potentiometry were used. Three-dimensional graphs on the basis of the functional dependence of the apparent electrode potentials of the metals and alloys, temperature and the atomic number of the elements in the Periodic Table were obtained. The universal mathematical Maple 17 software was used for this purpose. Low values of the activity coefficients (10^{-12}–10^{-15}) show strong interaction between lanthanides and the liquid metal compositions. It was found that the activity coefficients depend from the atomic number of the element in the Periodic Table and shift towards to more ideal behavior with the temperature increasing.

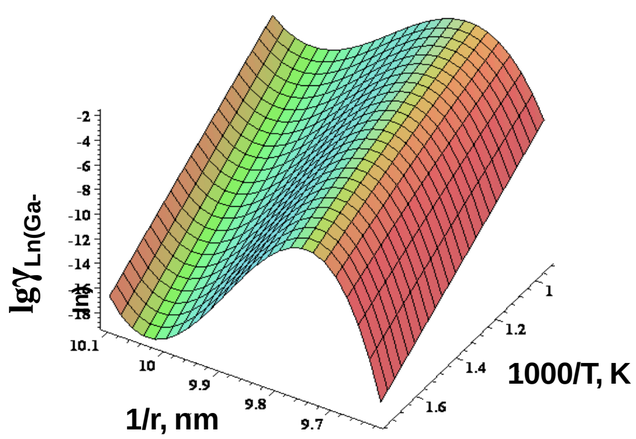

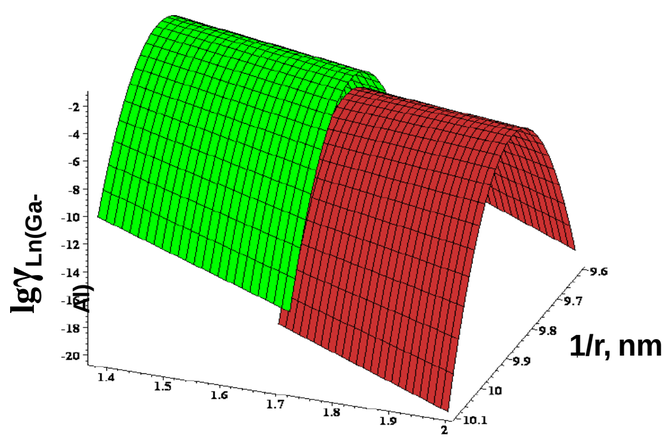

following scheme:

$$x[LnCl_6]^{3-} + 3\bar{e} + yGa + zMe = Ln_x$$

where Me is Al or In.

Analysis of the data obtained showed that Ga–In and Ga–Al alloys are the prospective media for application in partitioning technologies of spent nuclear fuels and nuclear wastes treatment.

The research was carried out with the financial support of the Russian Foundation for Basic Research in the framework of scientific project No. 20-03-00743.

IV International Conference and School "Advanced High Entropy Materials"
September 26-30, 2022

№ 41

ozerov@bsu.edu.ru

EFFECT OF HARDENING WITH BORIDES ON THE MICROSTRUCTURE AND MECHANICAL PROPERTIES OF TiNbZr AND $Al_5Nb_{24}Ti_{40}V_5Zr_{26}$ ALLOY-BASED COMPOSITES

Ozerov M. S., Sokolovsky V.S., Stepanov N. D., Zherebtsov S. V.

The aim: Establish the effect of strengthening with borides on microstructure and mechanical properties of the medium and high entropy alloy-based metal-matrix composites with different amounts of TiB_2 obtained by vacuum arc melting process

Microstructure

Alloy A — TiNbZr — 0.2 % wt. TiB_2

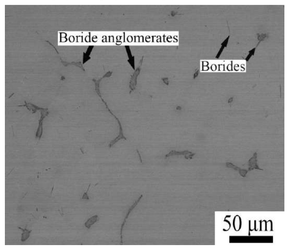

Alloy B — TiNbZr — 0.7 % wt. TiB_2

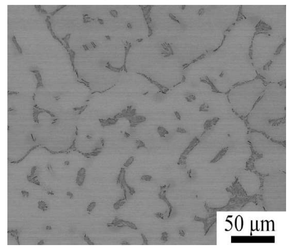

Alloy C — TiNbZr — 2 % wt. TiB_2

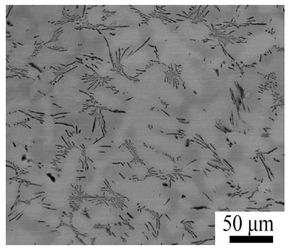

Alloy D — TiNbZr — 4 % wt. TiB_2

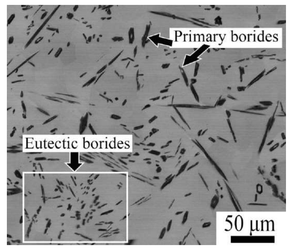

Alloy A — $Al_5Nb_{24}Ti_{40}V_5Zr_{26}$ — 1 % wt. TiB_2

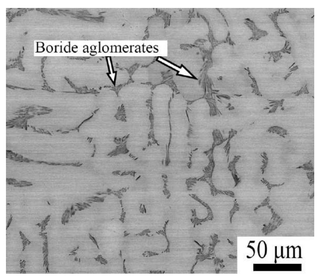

Alloy B — $Al_5Nb_{24}Ti_{40}V_5Zr_{26}$ — 2 % wt. TiB_2

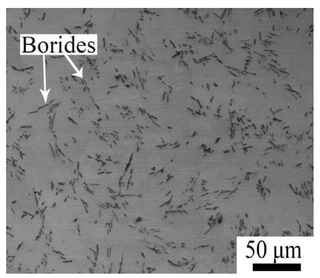

Alloy C — $Al_5Nb_{24}Ti_{40}V_5Zr_{26}$ — 3 % wt. TiB_2

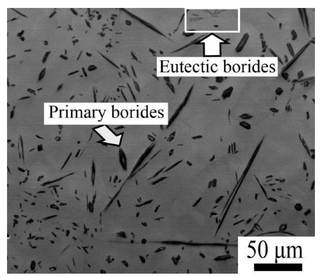

SEM-EDS mapping

distribution among the borides of

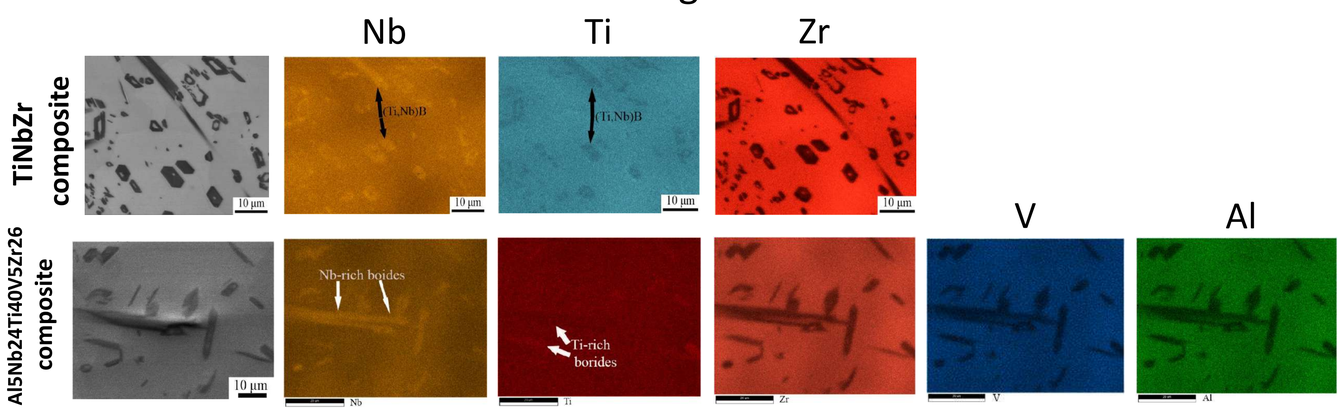

Mechanical properties

Tensile testing at room temperature

$TiNbZr - TiB_2$

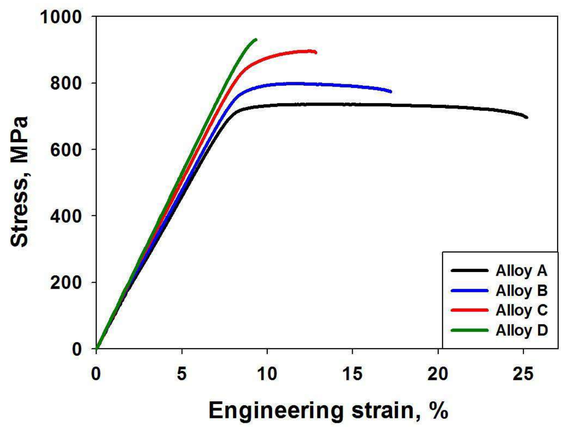

Composites	Yield strength, MPa	δ,%
Alloy A	690	20
Alloy B	750	10
Alloy C	810	5
Alloy D	900	0.5

$Al_5Nb_{24}Ti_{40}V_5Zr_{26} - TiB_2$

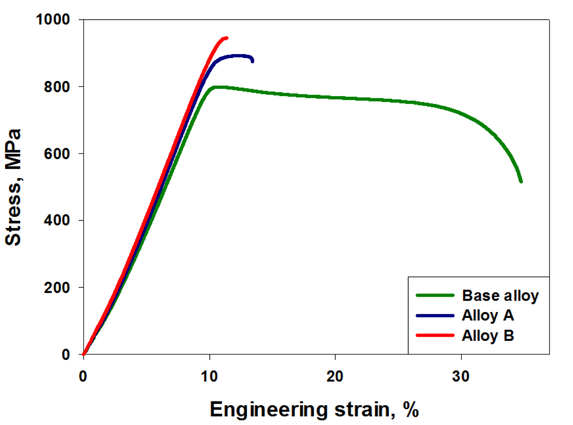

Composites	Yield strength, MPa	δ,%
Base alloy	760	29
Alloy A	840	5
Alloy B	890	0.5
Alloy C	900	0

Conclusions

1. The as-cast structures of the medium and high entropy alloy-based composites were composed of bcc matrix and (Ti, Nb) B needle-like borides;
2. A significant refinement of the bcc grain size was found with an increase in the proportion of borides;
3. The strength of the composites increased with increasing volume fractions of (Ti, Nb) B reinforcement.

Acknowledgment. The authors gratefully acknowledge the financial support from the grant of the President of Russian Federation (Grant No. МК-378.2022.4)

IV International Conference and School "Advanced High Entropy Materials" September 26-30, 2022

№43

OXIDATION RESISTANCE OF (NiCoFeCuMn)3(AlTi) HIGH ENTROPY INTERMETALLIC COMPOUND

ostovarim@susu.ru

Ostovari Moghaddam A., Sudarikov M., Mikhailov D., Trofimov E. A.

[1] South Ural State University, Chelyabinsk, Russian Federation

1- Introduction

High entropy intermetallic compounds (HEICs) are the most recent poster child of high entropy materials (HEMs) with potentially intricate properties since they combine the high entropy effects of solid solutions and the ordered crystal structures of intermetallic compounds. Recently, several HEICs with C14 Laves phase [1, 2], D022-phase [3], B2-ordered structure [4, 5], and σ-phase [2] have been developed. While research on HEICs is still in its infancy, several promising properties such as superior strength and thermal stability [3, 5], and exceptional oxidation resistance [6] have been already reported. Compared with binary intermetallics, HEICs even provide greater opportunity to further tailor their mechanical properties. For example, an interesting approach to provide better room-temperature ductility in intermetallics is production of two-phase or three phase microstructure with a mixture of ductile and ordered intermetallic phases, as we recently demonstrated in (NiCoFeCuMn)3(AlTi) HEIC [2]. In this work, we study high temperature oxidation resistance of (NiCoFeCuMn)3(AlTi) HEIC to further evaluate its performance for practical applications.

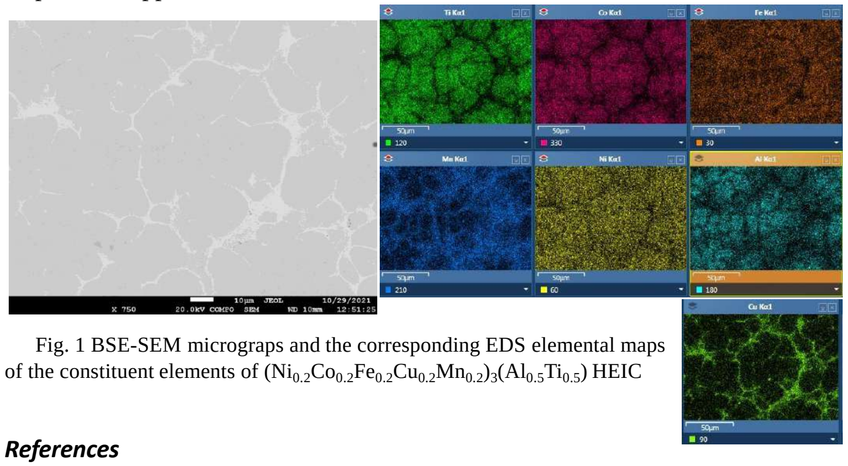

Fig. 1 BSE-SEM micrographs and the corresponding EDS elemental maps of the constituent elements of $(Ni_{0.2}Co_{0.2}Fe_{0.2}Cu_{0.2}Mn_{0.2})_3(Al_{0.5}Ti_{0.5})$ HEIC

2- Experimental

$(Ni_{0.2}Co_{0.2}Fe_{0.2}Cu_{0.2}Mn_{0.2})_3(Al_{0.5}Ti_{0.5})$ HEIC was prepared via milling followed by melting process. High purity (> 99.9 wt. %, Alfa-Aesar) precursor powders were first weighed according to the stoichiometric composition, thoroughly mixed via ball milling for 1 h, and then melted inside an induction furnace under reducing atmosphere. A 15-minutes soaking time was used to increase the homogeneity of the samples. Finally, the samples were taken out of the furnace and cooled to room temperature in laboratory atmosphere. The sample was then cut and polished for structural analysis. X-ray diffraction (XRD) was performed on a Rigaku Ultima IV X-ray diffractometer. Microstructural analysis was studied on a scanning electron microscope (SEM) Jeol JSM7001F equipped with energy-dispersive X-ray spectroscopy detector (EDS; Oxford INCA X-max 80). Quantitative oxidation resistance of the samples were measured using a Q-1500D derivatograph (Paulik and Erdei, Hungary) under isothermal conditions at 900 ºC for 10 h in air atmosphere. To reveal the oxidation behavior of the materials, the oxidized surfaces were then thoroughly analyzed by XRD and SEM-EDS analysis.

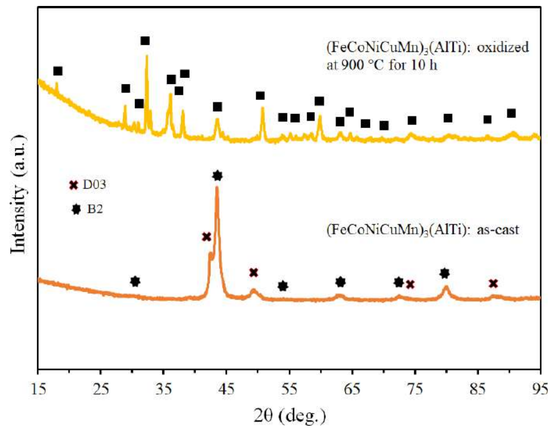

Fig. 2 XRD patterns of the as-cast and oxidized HEIC

3- Results and discussion

In this study, we investigated the oxidation resistance of $(Ni_{0.2}Co_{0.2}Fe_{0.2}Cu_{0.2}Mn_{0.2})_3(Al_{0.5}Ti_{0.5})$ HEIC at high temperatures to further examine the formation of complex oxides layer on its surface.

A clear segregation can be observed in $(Fe_{0.2}Co_{0.2}Ni_{0.2}Cu_{0.2}Mn_{0.2})_3(Al_{0.5}Ti_{0.5})$ HEIC, where Cu highly partitions in bright regions, Fe partially segregates adjacent to Cu, and Mn segregates along with Cu and Fe, creating an interconnected network microstructure (Figure 1). XRD spectra of this sample could be fitted by a B2 and a D03-type structures, suggesting the segregated regions crystallized into cubic D03 structure (A3B composition) with probably slightly different lattice parameters (Figure 2). The oxidation behavior of (NiCoFeCuMn)3(AlTi) at 900 °C was characterized by continuous weight gain without exhibiting a plateau region on the dynamic oxidation curve. The scale layer was mainly consisted of Mn oxide (Mn3O4) which could not provide an effective protection against high temperature oxidation (Figures 2, 3). Finally, it can be concluded that while phase segregation is effective to improve ductility of HEICs, it may have detrimental effect on their high temperature oxidation resistance.

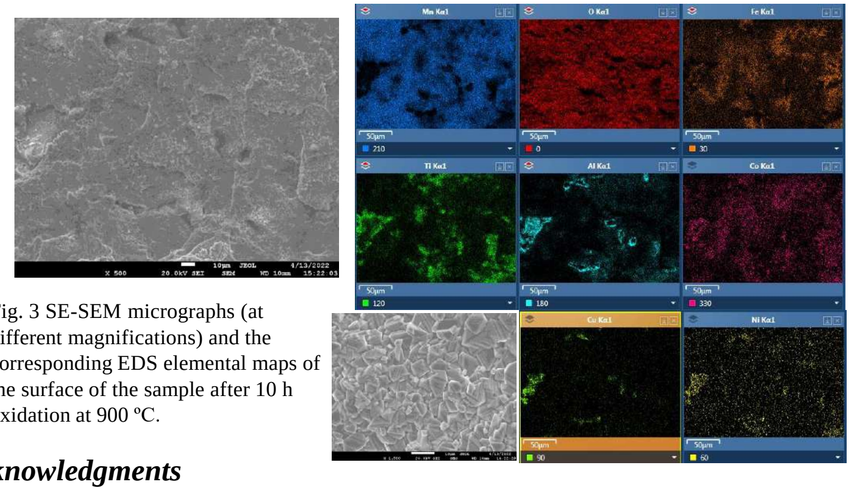

Fig. 3 SE-SEM micrographs (at different magnifications) and the corresponding EDS elemental maps of the surface of the sample after 10 h oxidation at 900 ºC.

References

[1] A. Ostovari Moghaddam, R. Fereidonnejad, D. Mikhailov, E. Trofimov, Mater. Lett., 132161 (2022).
2 A. Ostovari Moghaddam, D. Mikhailov, R. Fereidonnejad, N. Shaburova, D. Vinnik, D. Uchaev, F.-Q. Bai, D. Janas, E. Trofimov, J. Alloys Compd., 912, 165195 (2022).
3 A. Ostovari Moghaddam, A. Abdollahzadeh, M. Samodurova, N. Shaburova, D. Mikhailov, R. Fereidonnejad, V. Zhivulin, E. Trofimov, Intermetallics, 146, 107591 (2022).
4 A. Ostovari Moghaddam, R. Fereidonnejad, D. Mikhailov, E. Trofimov, Mater. Lett., 132161 (2022)
5 K. Yao, L. Liu, J. Ren, Y. Guo, Y. Liu, Y. Cao, R. Feng, F. Wu, J. Qi, J. Luo, Scripta Mater., 194, 113674 (2021). ; [6] L. Liu, L. Zhang, D. Liu, Scripta Mater., 189, 25-29 (2020).

Acknowledgments

The work was supported by the Russian Science Foundation, project No. 21-73-00086.

dimmak-panov@mail.ru

EFFECT OF ROTARY SWAGING AND SUBSEQUENT ANNEALING ON THE STRUCTURE AND MECHANICAL PROPERTIES OF A METASTABLE AUSTENITIC STAINLESS STEEL

Panov D.O., Kudryavtsev E.A., Chernichenko R.S., Naumov S.V.
Belgorod State University, Belgorod, Russia

Metastable austenitic stainless steels (MASS) possess high ductility, impact toughness, and corrosion resistance but reduced yield strength. Obtaining a gradient structure resulted in an increase in strength without a noticeable decrease in ductility and impact toughness. Using laboratory techniques and small samples, gradient structures with 200 microns in depth are usually attained. Thereby, it is difficult to apply these approaches for real products. However, rotary swaging with high strain might result in the bulk structural gradient formation. Subsequent heat treatment can be accompanied by reverse martensitic transformation, polygonization, recrystallization, and precipitation of nanoparticles that can change mechanical properties in the wide range. Thus, the present work aims to study the effect of rotary swaging and subsequent heat treatment on the structure and mechanical properties of a metastable austenitic stainless steel.

During cold rotary swaging of the AISI 321 steel rod with a strain of 60% or more, the formation of the strong gradient structure occurs that is associated with a gradual increase in the α'-phase fraction in the radial direction from the rod center to the edge (Fig. 1a). The most pronounced gradient structure is formed after a strain of 90%. Meanwhile, the texture gradient of austenite is also obtained. So, in the center, the strong two-component axial 111// rod axis (RA) and 001//RA texture is found that sufficiently diffused towards the edge. After cold rotary swaging, UTS and YS increase from 610 to 1410 MPa and from 270 to 1405 MPa, respectively (Table 1). Yet, ultimate elongation and impact toughness decrease from 67 to 11.5% and from 1.58 to 0.7 MJ/m^2, respectively.

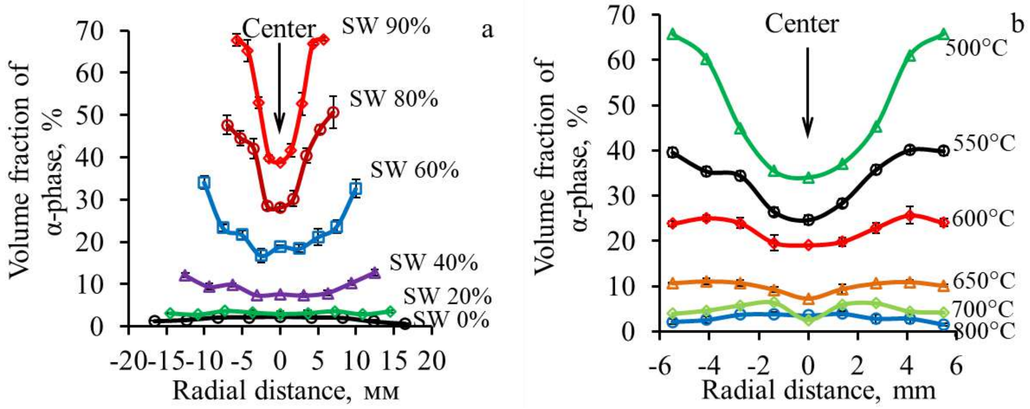

Figure 1. Distribution of the α-phase along the bar diameter after (a) cold radial forging and (b) subsequent annealing at different temperatures (after a 90% swaging reduction)

Table 1. Mechanical properties of the program steel after different treatment modes

Treatment mode	σ_B, MPa	$\sigma_{0,2}$, MPa	δ, %	ψ, %	KCT, MJ/m^2
Initial	610	270	66	74	1,58
Swaging 20%	755	735	38	67	0,9
Swaging 40%	1020	1010	16	59	0,65
Swaging 60%	1160	1150	13	54	0,64
Swaging 80%	1350	1330	12	46	0,66
Swaging 90%	1410	1405	11	39	0,69
Swaging 90% + Annealing 500°C	1545	1430	9	42	1,41
Swaging 90% + Annealing 550°C	1335	1140	15	51	0,76
Swaging 90% + Annealing 600°C	1210	965	19	55	1,01
Swaging 90% + Annealing 650°C	1150	905	21	57	1,25
Swaging 90% + Annealing 700°C	975	725	24	48	0,64
Swaging 90% + Annealing 800°C	735	355	385	60	0,95

During low-temperature annealing (500-650 °C), partial reverse martensitic transformation, uncompleted recrystallization and nanocarbide precipitation are observed. At the same time, the structural and textural gradients, as well as the gradient of the α'-phase fraction (Fig. 1b), are unchanged. Medium-temperature annealing (700 °C) is accompanied by a decrease in the α'-phase fraction to the level of the undeformed condition (2-5%), but recrystallization is also not finished. After high-temperature annealing (800-900 °C), the reverse martensitic transformation and recrystallization are completed and the equiaxial austenitic structure is formed. It should be noted that the excellent mechanical properties are received after low-temperature annealing at 500 and 650 °C. After annealing at 500 °C, the strength characteristics and impact strength increase by ~ 10% and 2 times, respectively, in comparison with the cold-swaged condition (Table 1). However, after annealing at 650 °C, the improved level of strength characteristics, plasticity and toughness is observed.

This research was funded by the Russian Science Foundation Grant no. 20-79-10094.

Boreskov Institute of Catalysis

IV International Conference and School "Advanced High Entropy Materials« September 26-30, 2022

№45

mishakov@catalysis.ru

Pervikov A.V., Pustovalov A.V., Bauman Y.I., Potylitsyna A.R., Afonnikova S.D., Volodin A.M., Mishakov I.V.

CATALYTIC GROWTH OF CARBON NANOMATERIALS ON MULTICOMPONENT ALLOYS PRODUCED BY JOINT ELECTRIC EXPLOSION OF WIRES

The aim: develop a method for obtaining two- and five-component alloys and to compare their catalytic ability in the decomposition of hydrocarbons with the production of carbon nanofibers (CNFs).

Motivation

The synthesis and study of carbon nanomaterials (CNMs) is one of the promising areas of modern materials science. The structure of CNM and their functional properties are determined by the nature of carbon-containing raw materials, the parameters of the catalytic decomposition process, and the composition of the used catalyst. The basis of the catalysts used for CNM synthesis are mainly metals of the iron triad (Fe, Co, Ni) capable of synthesizing carbon filaments by the carbide cycle mechanism. Alloy additives (Pd, Cu, Mo, etc.) are often used to increase the activity and stability of catalysts, which also significantly affect the structural characteristics of CNM.

Materials and methods

The key components in the composition of the alloys were Ni and Al. The alloy samples were obtained by joint exploding wires (EW). A mixture of C_2-C_4 hydrocarbons was used as hydrocarbon raw material. The process temperature was 600°C, reaction time - 30 minutes.

Three series of two- and five-component alloys of the following composition were obtained: $Ni_{95-75}Al_{25-5}$ (1), $Ni_{33-25}Fe_{29-23}Cu_{23-8}Al_{35-8}Cr_{9-7}$ (2), $Ni_{32-23}Fe_{31-21}Cu_{25-19}Al_{22-12}Co_{9-6}$ (3). The average particle size of the obtained samples ranged from 40 to 60 nm. The samples of series (1) were solid solutions based on the *fcc* lattice of nickel. Samples of series (2) and (3), according to XRD data, were solid solutions based on *fcc* or *bcc* lattice.

Results

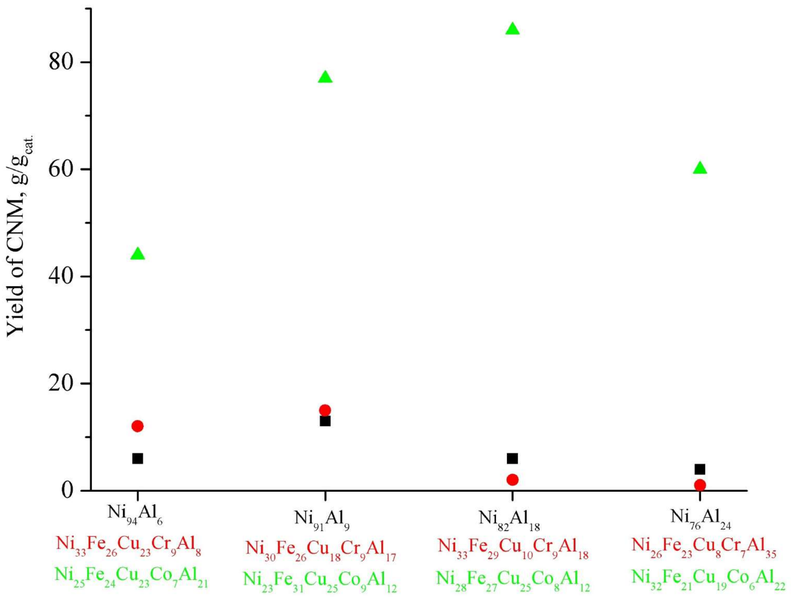

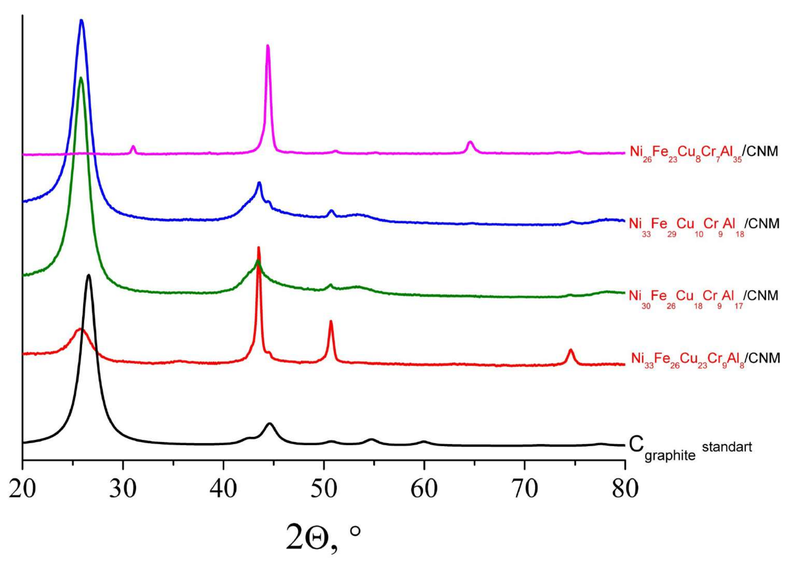

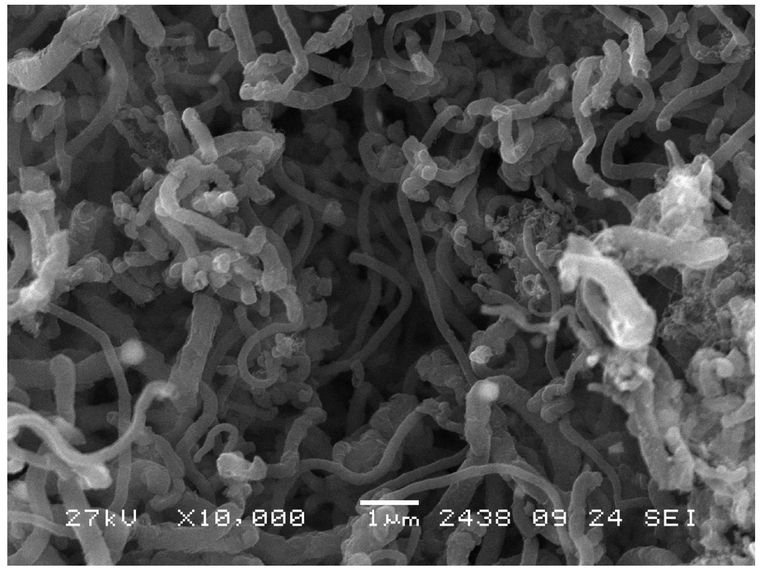

Acknowledgments. *The research was supported by the Russian Science Foundation (project No. 22-13-00406)*

IV International Conference and School "Advanced High Entropy Materials"
September 26-30, 2022

№46

petrov@ism.ac.ru

STUDY OF THE MOTION VELOCITY OF W AND TIC PARTICLES DURING HIGH-ENERGY TREATING OF A BARRIER

Petrov E. V., Kopytskiy V.O., Trofimov V.S.
Merzhanov Institute of Structural Macrokinetics and Materials Science Russian Academy of Sciences, Chernogolovka, Russia

In the process of high-energy interaction of detonation products in an explosive wave with powder particles, their entrainment occurs as a result of inelastic collision of detonation product molecules with particles. The collision of the particle flow with the barrier leads to the stoppage of the largest part of them in the near-surface zone and the formation of a coating on its surface. Structural changes in the studied material consist of the action of shock waves created when a particle flow collides with a barrier, and from the effect of particles embedded in the sample.

In the experiments, samples of U8 tool steel with a diameter of 25 mm and a height of 30 mm was used as a steel barrier, as well as powders of tungsten (10-16 microns) and titanium carbide (50-70 microns). Bulk density hexogen was used as an explosive.

After the detonation began, the shock wave and the detonation products of the explosive dispersed the powder particles (m = 5 g.) in the guide channel and together with them affected the barrier.

The arrangement of the experiment is shown in Figure 1. The test sample (6) was placed in a guiding plexiglas channel (5), on top of which a ring (3) with powder (4) with a bulk density of 5 g was located. A plate-cutter (2) was mounted on the ring, so that the detonation products outside the guiding channel did not close the field of view for the four-channel electron-optical camera Nanogate-4BP. An explosive (1), hexogen of bulk density, was placed on top of the plate. The length-diameter ratio of the explosive was 2.85, which corresponds to the condition for the initiation of a stationary detonation wave [1], and the parameters of the detonation wave and the reaction time in its front are independent of the explosive length. An air gap was left between the powder and the explosive to ensure a longer loading of the powder particles and form a plane shock front. The experimental assembly was placed in an explosive chamber and the electron-optical camera recorded the experiment through a protective window due to the presence of explosion damaging factors and gaseous detonation products.

An electron-optical camera Nanogate-4BP for high-speed photo shooting, which allows taking four frames in one experiment, was used (fig. 2). The delay time for the start of taking the first frame after the detonation of the explosive was 7 microseconds, which is necessary for the detonation products to reach the powder layer. The delay time between frames is 5 microseconds.

Analysis of high-speed photographs of the movement of powder particles and explosive detonation products in the guide channel showed that the flow of tungsten particles moves at an average speed of 2.4 km/s; the flow of titanium carbide particles at a speed of 4.9 km/s.

Experiments

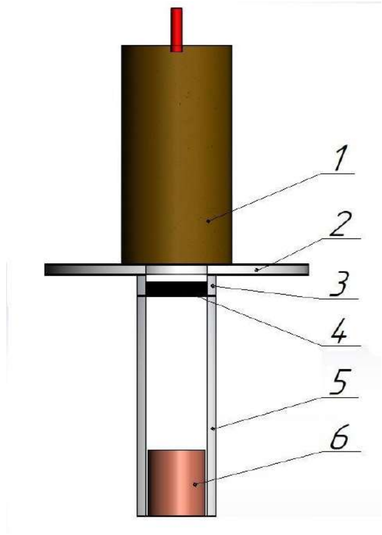

Fig. 1. Experimental scheme
1 – explosive; 2 – plate-cutter;
3 – fixing ring; 4 – powder;
5 – guiding plexiglass channel;
6 – sample.

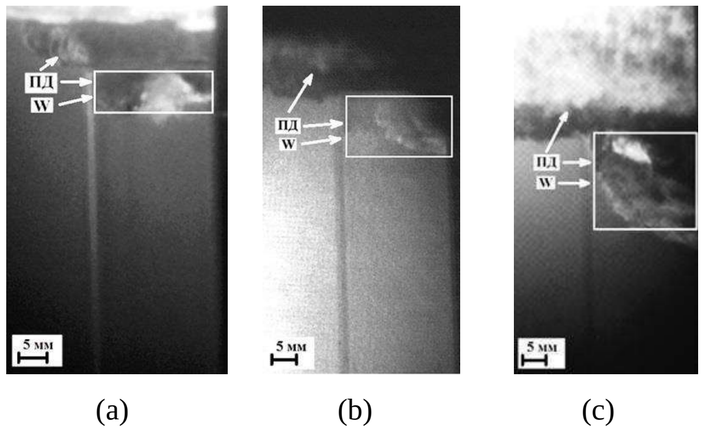

(a) (b) (c)

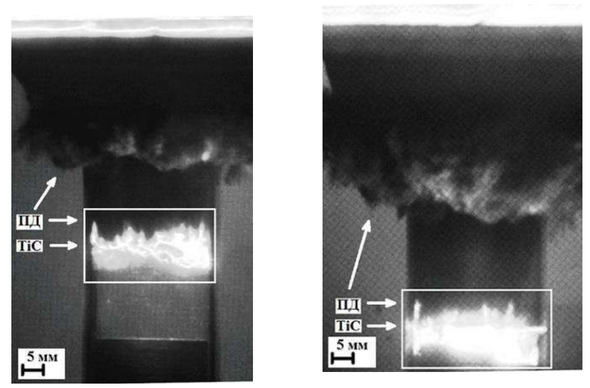

(d) (e)

Fig. 2. Frames of the movement process of tungsten particles: a) first frame; b) second frame; c) third frame; and titanium carbide: d) second frame; e) third frame; dispersed by explosive, inside the guide channel.

References

1. Dremin A.N., Savrov S.D., Trofimov V.S., Shvedov K.K. 1970 Detonation waves in condensed matter. Moscow, Science Press, 1970. 164 p.

IV International Conference and School "Advanced High Entropy Materials"
September 26-30, 2022

№47

help@ism.ac.ru

POLYMETALLIC GRID CATALYSTS WITH ACTIVATED SURFACE FOR THE SYNTHESIS OF CARBON NANOTUBES FROM METHANE

Pugacheva E.V., Zhuk S. Ya., Borshch V. N.

Merzhanov Institute of Structural Macrokinetics and Materials Science of RAS

In this work, we show the possibility of obtaining of carbon nanotubes (CNT) on nichrom grid polymetallic catalyst with a 0.5 ×0.5 mm cells and wire diameter of 0.3 mm. Initial grid samples were degreased and aluminized by being covered with ASD-1 aluminum powder and subsequent keeping at 620°C under argon for 4 h. The samples taken out after calcination were leached in a solution of NaOH, and stabilized in a solution of H_2O_2. The surface of the thus obtained catalysts was covered with nanoformations. Methane was used as the feedstock for pyrolysis. Even at a low conversion of the initial methane in the temperature range of 600–700°C, the formation of a significant amount of CNT on the surface of the catalytic grid was observed. Obtained CNT have a specific surface area of 141.2 m^2/g. The composition contains an admixture of nickel.

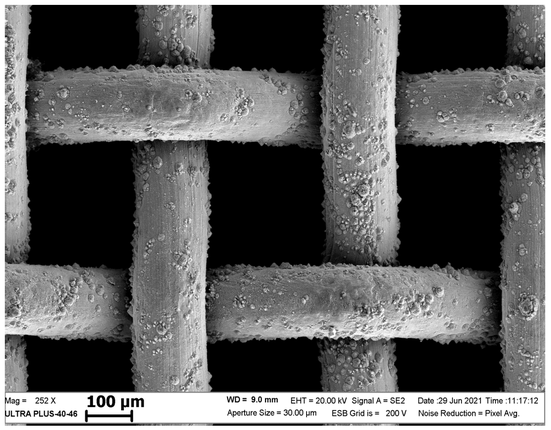

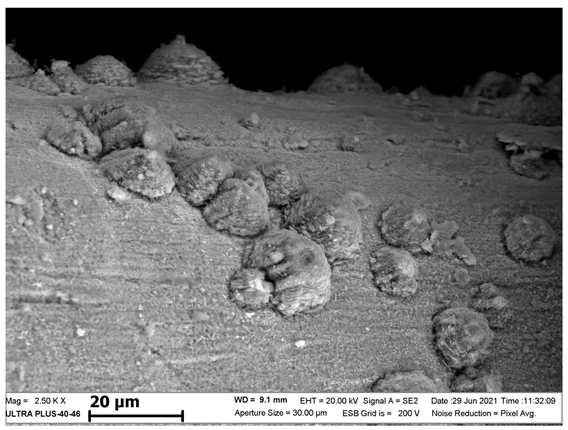

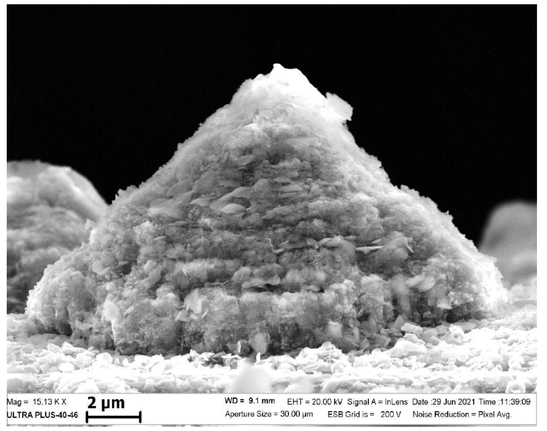

SEM images of the surface of nichrom grid after activation.

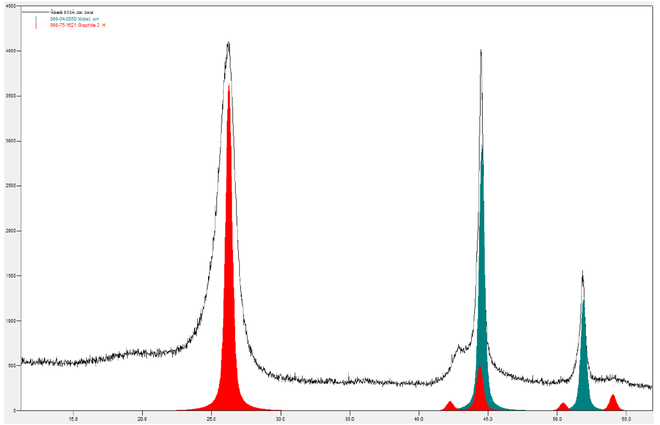

XRD of obtained CNT.

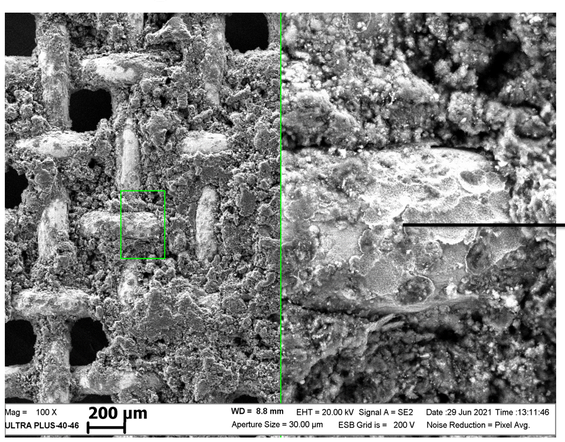

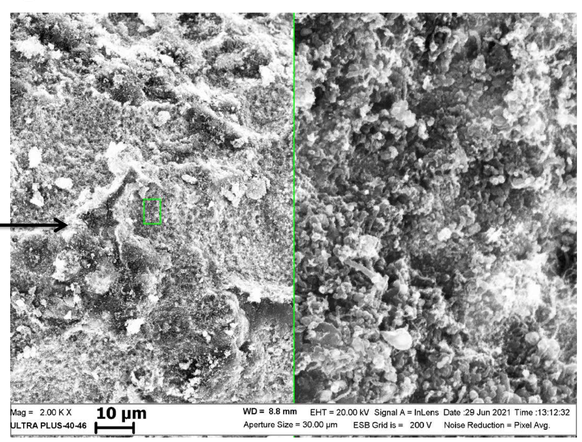

SEM images of the surface of nichrom grid after CNT synthesis.

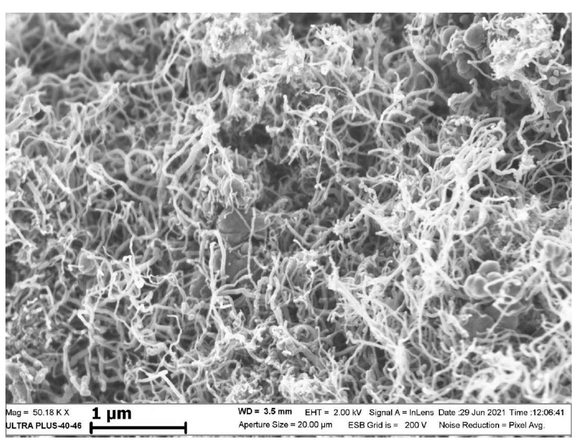

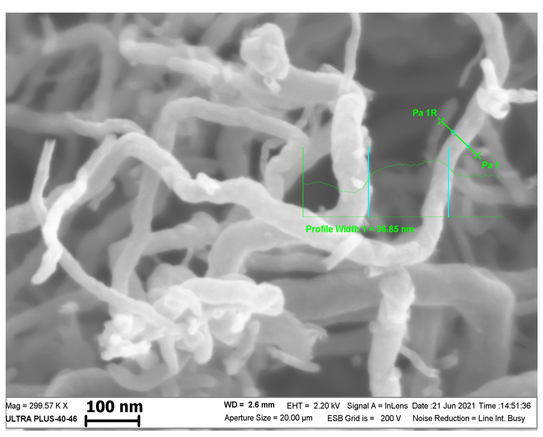

SEM images showing the surface of CNT.

IV International Conference and School "Advanced High Entropy Materials"
September 26-30, 2022

№48

help@ism.ac.ru

SYNTHESIS AND INVESTIGATION OF Ni/TiC AND Ni-Co/TiC CATALYSTS FOR CO_2 HYDROGENATION TO METHANE

Pugacheva E.V., Zhuk S. Ya., Borshch V. N., Kochetkov R. A., Seplyarskii B. S.
Merzhanov Institute of Structural Macrokinetics and Materials Science of RAS

Synthesis of the catalysts DI and DII, and precursors PII, PII and PIII from granulated mixtures Ti+C+Ni(+Co+Al)

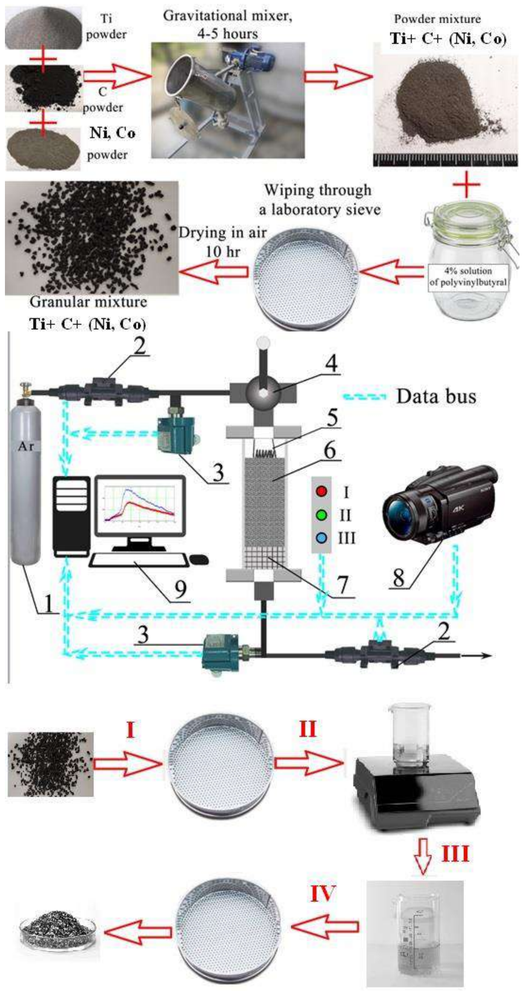

Synthesis of the catalysts LI, LII, LIII and LIV from precursors:

I. 0.6–1.6-mm precursors were crushed to 0.1-0.3 mm fraction

II. leaching with 20% NaOH solution (spontaneous reaction for 1 h, boiling for 1 h, and holding at room temperature for 24 h)

III. wash-out and stabilization with 10% H_2O_2 solution (for 0.5 h)

IV. classification with fraction selection 0.1-0.3 mm

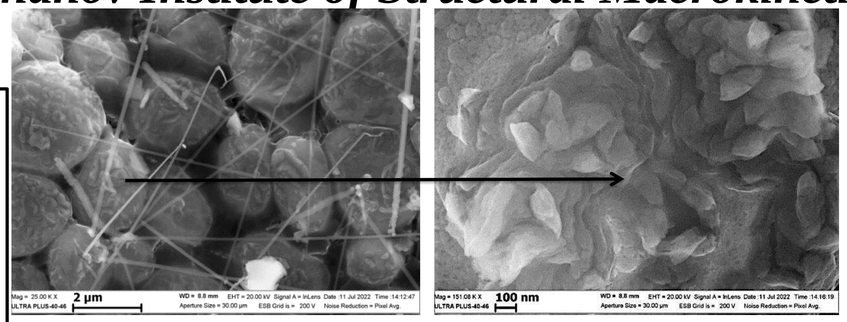

SEM images of the surface of granular precursor TiC + 20%wt.(Ni + Al), Ni : Al = 1 : 1

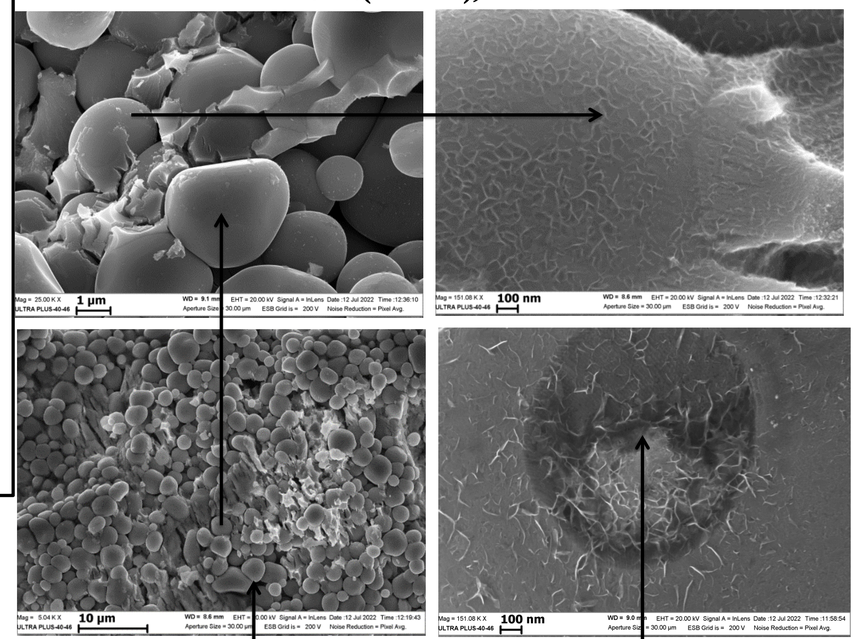

SEM images of the surface of granular catalyst 10%wt.Ni/TiC

SEM images of the surface of granular catalyst (4%wt.Ni+4%wt.Co)/TiC

Hydrogenation of CO_2 with gas mixtures: CO_2 5%+H_2 5n%, He the rest, n=1, 2, 3, 4. GHSV=6000 h^{-1}

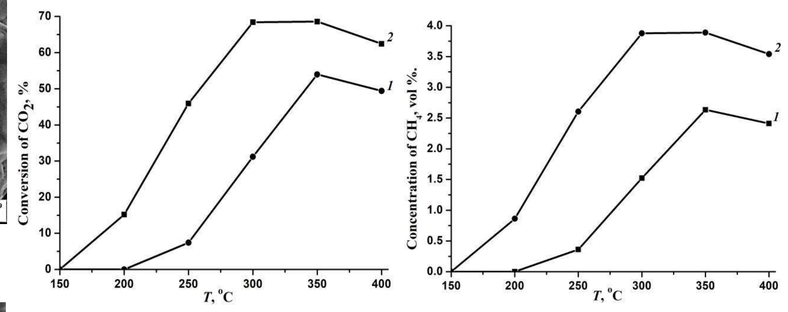

Conversion of CO_2 and yield of methane vs temperature over the catalyst 10%wt.Ni/TiC using gas mixtures with n=3 (1) and n=4 (2)

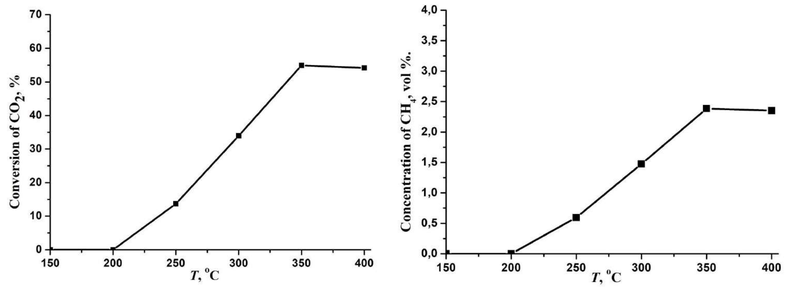

Conversion of CO_2 and yield of methane vs temperature over the catalyst (4%wt.Ni+4%wt.Co)/TiC using gas mixture with n=4

Precursors	Phase composition
PII, TiC + 20 wt % (Ni + Al), Ni : Al = 2 : 3	TiC_{cub}, $Ni_2Al_{3\ hex}$, $NiAl_{3\ ort}$
PIII, TiC + 30 wt % (Ni + Al), Ni : Al = 1 : 2	TiC_{cub}, Al_{cub}, $NiAl_{3\ ort}$

The main phases of direct synthesized catalysts DI and DII are TiC_{cub} and $Ni_{0.9}Ti_{0.1}$, for leached catalysts: TiC_{cub} and Ni_{cub} (Ni_{cub}+Co_{cub} for LIV)

Sample	Composition	Specific surface area, m^2/g
Catalyst DI	10%wt.Ni/TiC	2.8
Catalyst DII	20%wt.Ni/TiC	1.3
Precursor PI	TiC + 20%wt.(Ni + Al), Ni : Al = 1 : 1	1.2
Precursor PII	TiC + 20%wt.(Ni + Al), Ni : Al = 2 : 3	1.5
Precursor PIII	TiC + 30%wt.(Ni + Al), Ni : Al = 1 : 2	0.99
Catalyst LI	10%wt.Ni/TiC	1.3
Catalyst LII	8%wt.Ni/TiC	2.5
Catalyst LIII	10%wt.Ni/TiC	2.6
Catalyst LIV	(4%wt.Ni+4%wt.Co)/TiC	1.1

IV International Conference and School "Advanced High Entropy Materials"
September 26-30, 2022

№ 49

ASPECTS OF HIGH-SPEED PHOTOGRAPHY OF SHOCK-WAVE LOADING OF STEEL TUBE

galiev@ism.ac.ru

Galiev N.N[1]., Malakhov A. Yu.[1], Denisov I. V.[1], Seropyan S. A.[1], Shakhrai D. V.[2], Sosikov V. A.[2], Rapota D. Yu.[2,3]
[1]Merzhanov Institute of Structural Macrokinetics and Materials Science Russian Academy of Sciences, Chernogolovka, Russia
[2]Institute of problems of chemical physics of Russian academy of sciences, Chernogolovka, Russia
[3]Lomonosov Moscow State University, Moscow, Russia

Currently, the complex technology including SHS, shock-wave loading and extrusion is one of the promising technologies for the production of metal-intermetallic composites.

This study presents the results of high-speed photography of experiments on compression of a steel tube by an oblique shock wave. For high-speed photography, an electron-optical camera Nanogate 22/16 with a shooting frequency of 1 million frames/s was used.

Electron-optical camera Nanogate 22/16

The experiments were carried out according to two schemes using ammonite as an explosive. According to the first scheme, a hollow steel tube with a diameter of 14 mm and a length of 70 mm was compressed; in the second scheme, a tablet from a reactive Ni-Al powder mixture with a height of 10 mm was placed inside the lower part of the tube. The schemes provided for strong joint of the tube and the upper plate on which it was installed with the lower plate. The thickness of the lower plate was equal to 2 and 12 mm in the schemes No.1 and 2, respectively. To align the detonation front, a conical steel plug was installed in the top of the tube.

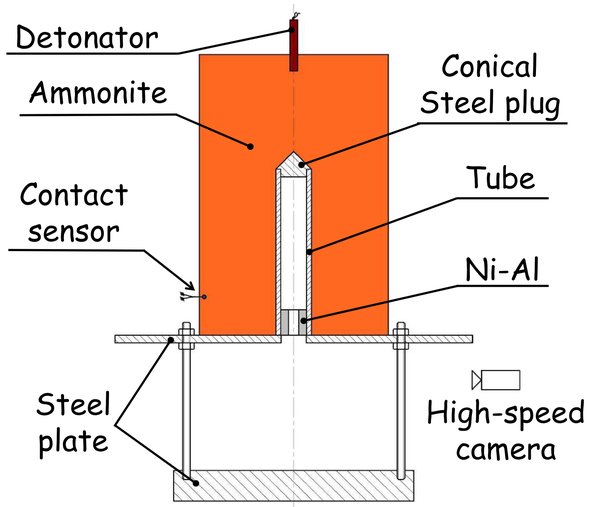

The second scheme diagram of experiment

A tablet from a reactive Ni-Al powder mixture

Real view of experimental scheme

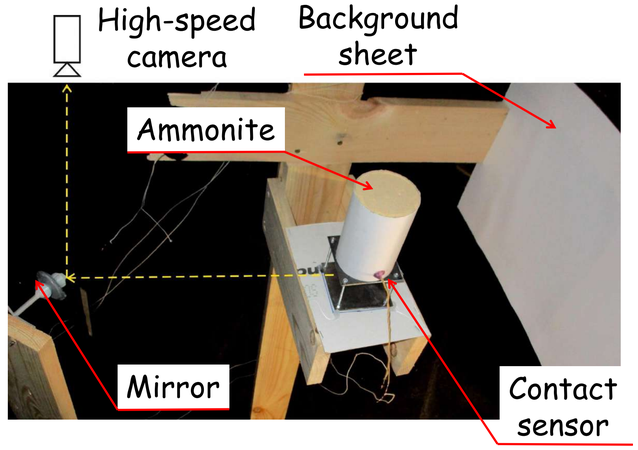

Experimental scheme assembly

The bottom steel plate after shock-wave loading according to the first scheme

The bottom steel plate after shock-wave loading according to the second scheme

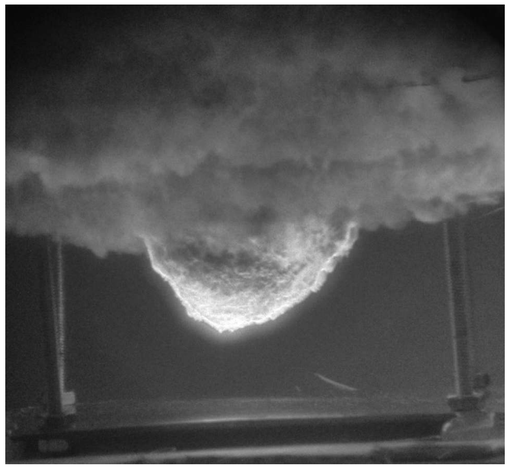

Last frame from experiment No.1 (delay - 0 μs)

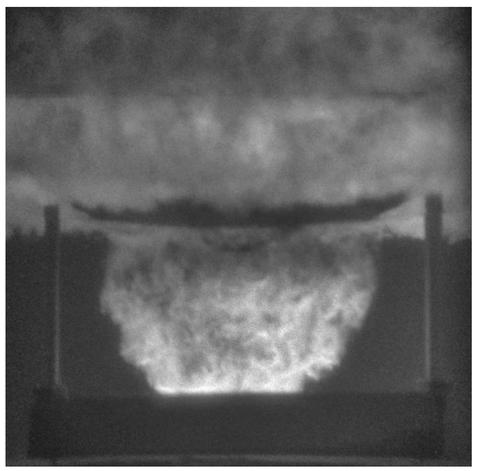

Last frame from experiment No.2 (delay - 5 μs)

Based on the results obtained, it can be concluded that it is promising to carry out further experimental work to study the characteristics of a high-speed flow of particles and gases formed as a result of shock-wave loading of the tube outer surface. The results obtained will be used to develop the technology of shock-wave extrusion of intermetallics and cermets in a metal shell.

IV International Conference and School "Advanced High Entropy Materials"
September 26-30, 2022

№ 50

E-mail: Russkih_a_s@mail.ru

STRUCTURE AND MECHANICAL PROPERTIES OF AL – TI – ZR – V - NB HIGH – ENTROPY ALLOYS OBTAINED BY ALUMATHERMY

Russkih A. S., Zhilina E. M., Krasikov S. A.
Institute of Metallurgy of the Ural Branch of the Russian Academy of Sciences, 101, Amundsen street, Ekaterinburg, Russia 620016

Two decades ago, a completely new concept appeared in the metallurgical field, it made possible to obtain a new type of materials - high-entropy alloys. Since the development of high-entropy alloys, the number of components in them has gradually increased, and their ratio has varied from 5 to 35 at. %. It should be noted that high-entropy alloys have unique physical and mechanical properties, in many ways superior to known superalloys such as Inconel 718 and Haynes 230. This paper presents the results of obtaining a high–entropy Al – Ti – Zr – V - Nb alloy by the method of aluminothermic reduction of metals from their oxides (TiO2, ZrO2, V2O5, Nb2O5) (fig1).

Fig.1 Results of melting oxides in an alund crucible

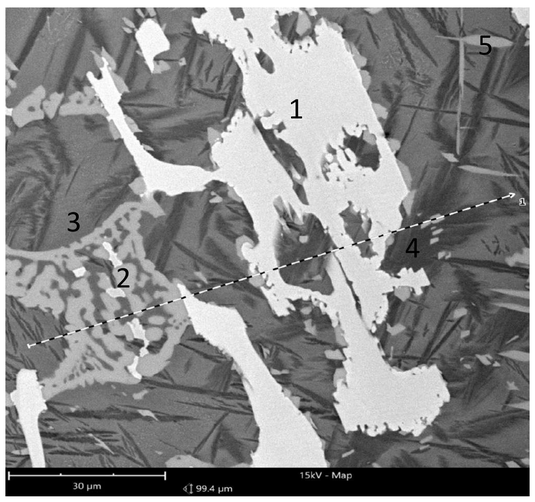

Fig. 3 – Results of microstructural analysis

The resulting alloy was studied by X-ray spectral microanalysis (XSMA), X-ray phase analysis (XPA). The microhardness of the samples was measured using the Vickers method. The load and exposure time did not exceed 200 kgf/mm2 and 15 seconds, respectively.

The chemical composition of the alloy is determined to be equal to (at. %): 26.28Al-15.92Ti-8.23Zr-26.57V-23Nb.

According to the XPA (fig. 2), the main phase is a solid solution Ti0.64V0.52Al0.84. The ZrVAl, TiAl, Ti1.5Zr1.5V2Al3, Nb3Ti2Al3 phases are also identified. The composition of the latter was confirmed by a full-profile analysis using the Rietveld method using as an initial model the structural parameters of the compound Ta5Al3, as closer than Zr5Al3.

The results of electron microscopy (Fig. 3) showed that there are five different regions in the alloy with the compositions shown in Table 2. It can be seen that phase 3 is the most common in the volume, where a significant amount of aluminum, titanium and vanadium is represented, which correlates with the obtained XRD results (phase 1, Table 1) and may relate to by phase Ti0.64 V0.52 Al0.84. Regions 1, 3 and 4 are also rich in niobium, which corresponds to phase 4 of the phase composition table.

Table 2 – Electron microscopy results for different areas (Figure 4)

	1		2		3		4		5	
Элемент	**ат. %**	**вес. %**	**ат. %**	**вес. %**	**ат. %**	**вес. %**	**ат. %**	**вес. %**	**ат. %**	**вес. %**
Nb	31.48	48.37	12.40	21.42	20.72	37.71	20.62	39.04	15.38	25.44
Zr	10.64	16.05	23.10	39.20	1.37	2.45	1.30	2.41	23.17	37.63
Ti	14.57	11.53	4.58	4.08	19.61	18.40	21.31	20.79	8.26	7.03
Al	24.74	11.04	48.38	24.28	35.67	18.86	43.36	23.84	41.64	20.00
V	11.63	9.79	10.63	10.08	22.63	22.59	13.41	13.92	10.17	9.22

List of references
1. *Pengfei Gu, Tengbo Qi, Lan Chen et al. // Int J Refract Hard Met. 2022. V.* ***105****. P. 105834*
2. *Bang Xiao, Wenpeng Jia, Huiping Tang et al. // J Mater Sci Technol. 2022. V.* ***108****. pp. 54-63*
3. *Lin Chen, Yueyi Wang, Xuanhong Hao et al. // J Mater Sci Technol. 2021. V.* ***183****. P. 109823*

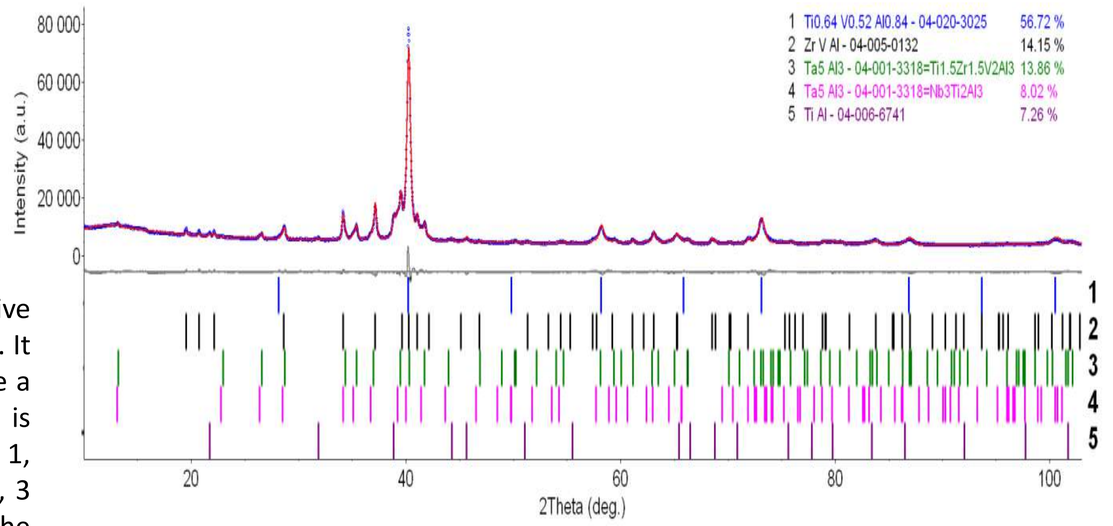

Fig. 2 Diffractogram of the alloy after the experiment

Table 2 Quantitative, qualitative phase composition

	Фаза	Прим.
1	$Ti_{0.64}V_{0.52}Al_{0.84}$	B2
2	Zr V Al	C14
3	$Ti_{1.5}Zr_{1.5}V_2Al_3$	типа Zr_5Al_3
4	$Nb_3Ti_2Al_3$	
5	Ti Al	

The measurement of the microhardness of the sample (Fig. 4) showed an average of 647.87 HV, similar values were obtained earlier for refractory wind turbines VNbMoTaW [1], WMoTaNbTi [2], AlNbTiMoV [3].

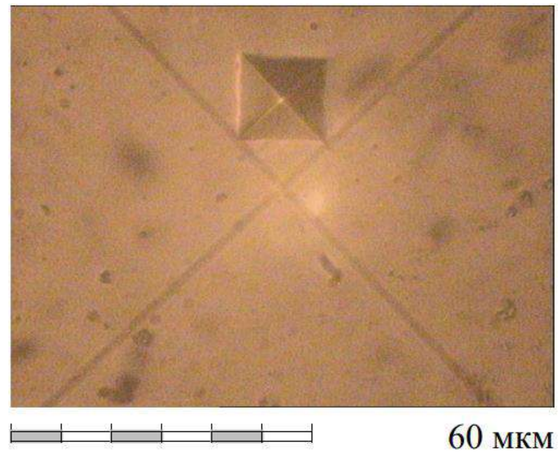

Fig. 4 Microhardness of Al-Ti-Zr-V-Nb alloy

The work was carried out according to the state assignment for IMET UB RAS (State registration number of the topic: 122020100404-2) using equipment of the Collaborative usage centre "Ural-M"

IV International Conference and School "Advanced High Entropy Materials"
September 26-30, 2022

№ 51

Salamvit@yandex.ru

Synthesis of single-phase $NBSi_2$ and Nb_5Si_3 in the mode of thermally coupled SHS processes

[1]Salamatov V. G., [1]Shchukin A. S., [1]Kovalev I. D. , [2]Shkoda O. A

1- ISMAN, 2-Tomsk Scientific Center

Introduction

Silicide of 5:3 (Nb/Si atomic ratio) compound is of great interest as high-temperature structural materials, mainly due to their high melting points (more than 2000 °C), low densities, and good mechanical strength at high temperatures. The disilicide of 1:2 (Nbl/Si atomic ratio) have found wide applications as thin films in microelectronics, as a result of their high electrical conductivity, high-temperature stability, corrosion resistance. [Materials Science and Engineering: A, Vol. 663, 29, 2016, Pages 98-107; Intermetallics, Vol. 46, 2014, Pages 72-79; Rare Metal Materials and Engineering, Vol. 44, Issue 1, 2015, 18-23].

Silicides of niobium have been produced by powder processes, with combination of hot pressing, hot isostatic pressing, reactive sintering, mechanical alloying, and plasma spraying [Journal of Alloys and Compounds, Vol. 826, 2020, 154228; Materials Characterization, Vol.191, 2022, 112098]. It is know high-velocity shock synthesis of niobium silicide using a granular niobium and silicon mixture prepared in atomic ratio of Nb5Si3 [Journal of Alloys and Compounds, Vol. 740, 2018, Pages 1032-1036].

With the advantages of time and energy savings, self-propagating high-temperature synthesis (SHS) has been considered as an alternative route to the conventional methods of producing advanced materials. It is well known that the thermal effect of the Nb with Si reaction is insufficient for its occurrence in an SHS mode. However, despite recent efforts, which have included to preheat the powder compact, field-activated, mechanical alloying, and mechanically activated, it remains challenging to create bulk single-phase NbxSiy by SHS. [Journal of Alloys and Compounds, Vol. 425, Issues 1–2, 2006, 216-222; Journal of Alloys and Compounds, Vol. 402, Issues 1–2, 27 2005, 118-123; Journal of Alloys and Compounds, Vol. 826, 2020]

This work aimed at checking out the applicability of thermally coupled SHS reactions to the synthesis NBSi2 and Nb5Si3 from elemental powders of Nb/Si.

Experimental

Niobium (< 45 μm, 99.8% purity), silicon (< 45 μm, 99.5% purity) and titanium (PTOM, < 63 μm, 99.7% purity) powders were used as the starting materials. Powder blends with two stoichiometric ratios Nb:Si = 5:3 and 1:2, Ti:Si = 5:3 were prepared by manual mixing Nb/Si and Ti/Si particles in a ceramic mortar for 30 min. Mixed powders were then cold-pressed into cylindrical sample compacts. The SHS experiments were conducted in a combustion chamber. The chamber was evacuated and filled with purity argon at $1.5 \cdot 10^5$Pa. The combustion process was observed using a tungsten-rhenium (A1 tape) thermocouple (T1-T3) of 100 μm thick. Thermocouples were installed (on 3 mm deep) in the samples. Thermocouples were coated with a 0.1–0.2 mm layer of thermo-resistant compound (BN powder in silicate glue). The signals of thermocouples were transmitted via an analog-to-digital converter to the computer.

The green density of the Nb-Si reactant compact was 70% of the theoretical maximum density (TMD) of the powder mixture and Ti-Si – 60 %. Diameter and mass of Nb-Si and Ti-Si compact were 12mm , 5 g and 30 mm, 15 g respectively. The DC electric tungsten spiral initiated a SHS wave in donor. Ashless filter paper (200 μm) was installed between Ti-Si and Nb-Si.

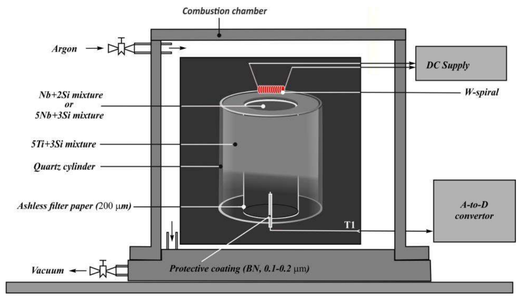

The green density of the Nb-Si reactant compact was 63 % of the theoretical maximum density (TMD) of the powder mixture and Ti-Si – 60 %. Diameter and mass of Nb-Si and Ti-Si compact were 30 mm , 20 g and 30 mm, 10 g respectively. The DC electric tungsten spiral and igniter Ti + 2B composition, evenly applied as a 1 mm layer on the 5Ti + 3Si mixture surface, initiated a SHS wave in donor. In order to provide better thermal contact, a set of donor and Nb-Si layers was tightened by using steel plates as shown in figure. Ashless filter paper (200 μm) was installed between layers of sandwich.

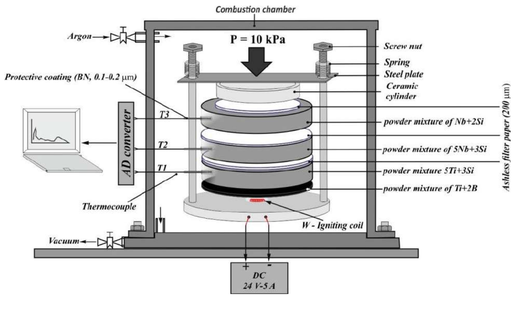

The obtained products were examined with X-ray diffraction analysis (DRON-3M with Cu-Kα radiation, database PDF-2) and scanning electron microscopy Carl Zeiss Ultra Plus .

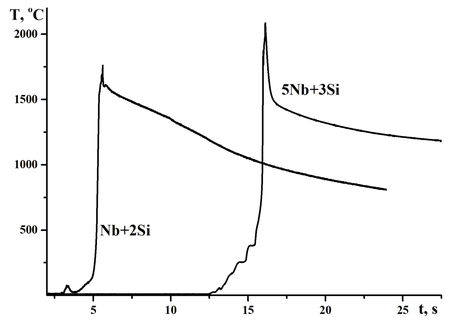

Typical combustion temperature profiles recorded from Nb–Si reactant

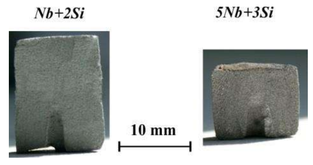

Images of products

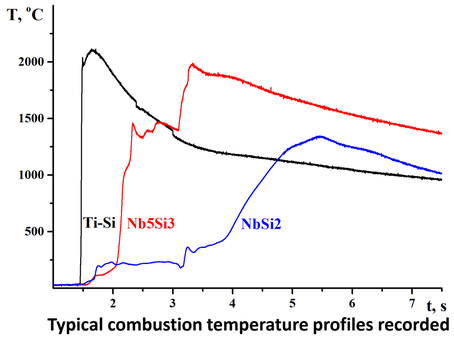

Typical combustion temperature profiles recorded from Nb–Si reactant compacts and Ti-Si.

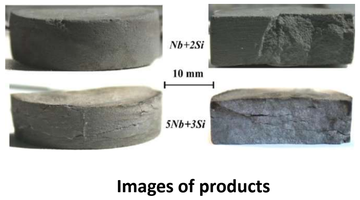

Images of products

Results

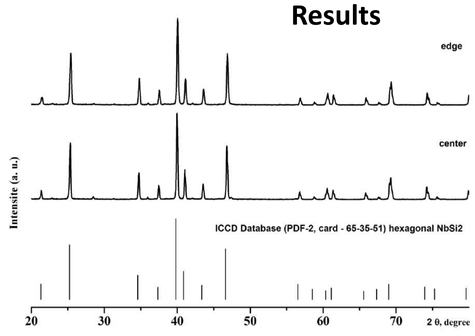

XRD patterns of combustion products obtained from sample compacts with Nb:Si = 1:2 and standard pattern for NbSi2

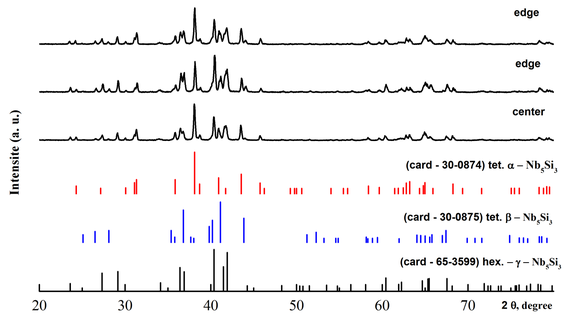

XRD patterns of combustion products obtained from sample compacts with Nb:Si = 5:3 and standard pattern for α, β, γ – Nb5Si3

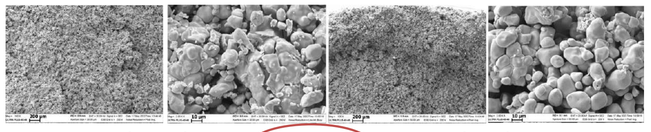

(center) Nb:Si = 1:2 (edge)

SEM images of products

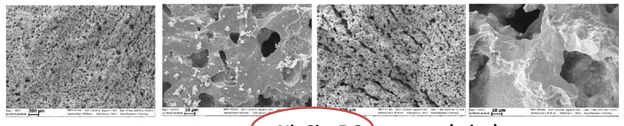

(center) Nb:Si = 5:3 (edge)

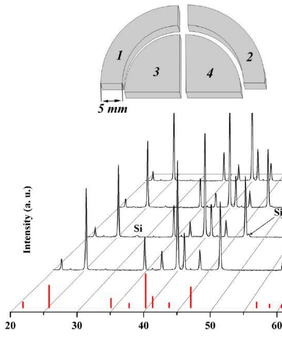

Abundance of NbSi2 (wt,%) - 12; a, b, g Nb5Si3 - 62, 19, 6; Nb3Si - 1

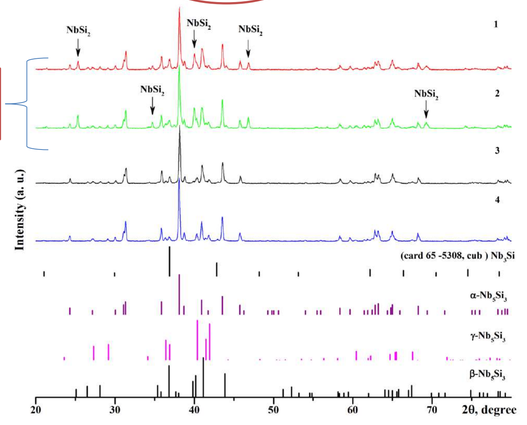

XRD patterns of combustion products obtained from sample compacts with Nb:Si = 1:2 and standard pattern for NbSi2

XRD patterns of combustion products obtained from sample compacts with Nb:Si = 5:3 and standard pattern for α, β, γ Nb5Si3, Nb3Si

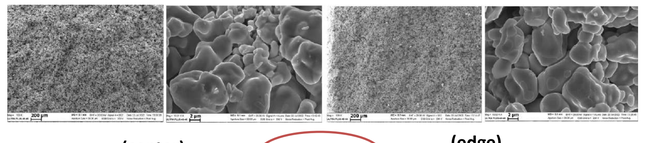

(center) Nb:Si = 1:2 (edge)

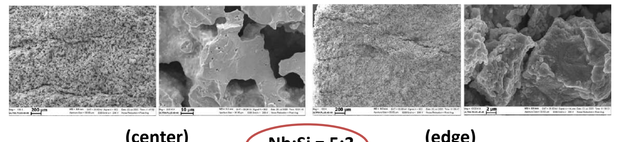

(center) Nb:Si = 5:3 (edge)

SEM images of products

IV International Conference and School "Advanced High Entropy Materials"
September 26-30, 2022

№ 53

TECHNOLOGY OF OXID-FREE HEATING OF CHIP-POWDE DISPERSIONS OF FERROUS METALS IN HOT BRIQUETTING FURNACES

niil_svarka@bntu.by

Belarusian National Technical University, Minsk, Republic of Belarus
Sereda V.U.

Heating and briquetting of metalworking wastes for the purpose of cleaning from coolant and remelting is associated with the issues of protecting the metal from oxidation, reducing waste and obtaining high-quality castings. In the technology proposed for implementation, heating is carried out in small-sized continuous muffle furnaces, the distinguishing feature of which is preheating in a gas burner flame to a temperature of 450...550 °C, then in a low-frequency inductor to a temperature of 700...800 °C. In this case, the metal is heated in an atmosphere of products of thermal sublimation and pyrolysis of the coolant without the access of an oxidizer with the release of coolant vapor into the burner flame. The pyrocarbon coating 0.1-0.2 mm thick formed on the surface of metal particles, in addition to protecting the metal from oxidation, acts as a lubricant in the hot pressing process. The high-calorific oil component of the coolant, entering the furnace furnace, burns together with natural gas.

The chips enter the induction heater in a practically dry form - the oil content is 4-5 wt.%. The charge is heated by direct contact heat exchange with the walls of the muffle, radiation and convection in the space of the muffle, which is especially effective when heating paramagnetic and non-magnetic materials that are part of metallurgical composites. Metal particles are also subject to electromagnetic influence. Due to the fact that contact heat exchange plays the main role in the heating process, the use of an energy-saving low-frequency inductor leads to significant energy savings. The metal comes out of the furnace completely free of coolant.

The device for implementing the method is a flow-through muffle furnace of the column type. The furnace consists of a loading device, gas-flame and induction heaters. The loading device is made in the form of a head 1 and a screw feeder 2. The gas-flame heater includes a shaft 3, a muffle 4, a screw 5 and a gas unit with a two-wire gas burner 6. The induction heater is made in the form of a copper water-cooled inductor 7 and a muffle 8. To remove gases from the furnace into the system of "wet" cleaning, neutralization and disposal, side chimneys b, vertical chimney c and hole d in the furnace shaft are used. The economic efficiency of hot briquetting is ensured by reducing the cost of electricity for the operation of the briquetting press, due to a decrease in the resistance of the metal to deformation by 2.0-2.2 times. The cost of natural gas is 10-12 times lower than the cost of electricity, and the content of the oil component of the coolant in the composition of the charge ensures a reduction in natural gas consumption by up to 30%. The formation of a pyrocarbon coating (lubricant) on the surface of metal particles reduces the work of a deformation seal by 10-15%. The release of solid carbon reduces the total amount of furnace gases and simplifies the task of their complete combustion.

The economic efficiency of hot briquetting increases many times with the use of sludge powders in the composition of the chips, as well as alloying additives in the production of composite charge materials of a given chemical composition. The composition of the charge may include fine fraction screenings of ferroalloys, flux and slag-forming additives: coke, lime, iron oxides, aluminum, silicon, split steel and cast iron shot, etc. Dense and high-strength briquettes with a predetermined and demanded chemical composition are sold at a higher selling price.

Figure 1. Carbon layer on the surface of steel chips

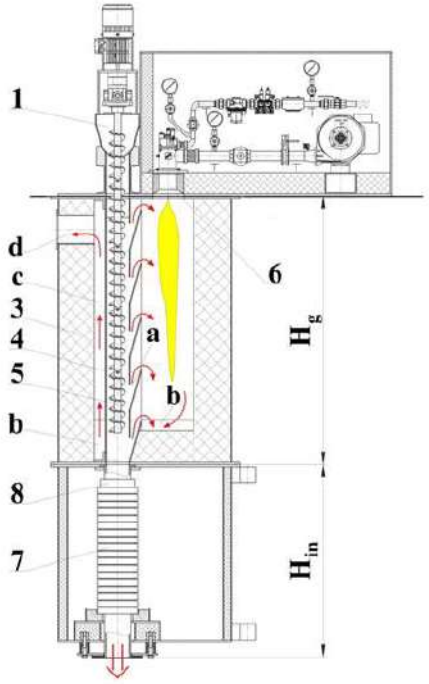

Figure 2. Schematic representation of a flow-through muffle furnace divided into heating zones: H_g -flame heating zone; H_{in} -induction heating zone.

IV International Conference and School "Advanced High Entropy Materials"
September 26-30, 2022

№ 54

stepan.seropyan@yandex.ru

INFLUENCE OF MECHANICAL ACTIVATION ON COMBUSTION PARAMETERS OF POWDER COMPACTS OF HF-PTFE AND HF-PTFE-AL SYSTEMS

Seropyan S. A., Saikov I. V., Saikova G. R.

Merzhanov Institute of Structural Macrokinetics and Materials Science Russian Academy of Sciences, Chernogolovka, Russia

Reactive materials are mixtures of metallic and non-metallic powders that, when subjected to high-speed impact or heating, release a large amount of thermal energy. These materials are used in the special purpose as cumulative liners and in the civil field for perforating oil wells.

Powders Hf (HFE-1), Al (ASD-1), with a particle size ≤ 50 μm and PTFE (Fluralite) a particle size < 5 μm were used in this work. Mechanical activation (MA) was carried out on an AGO-2 setup for 2 min at a speed of 2200 rpm. The ignition temperature was studied on cylindrical samples with a 3 mm in diameter and 1.5 mm high. The combustion rates and temperatures of the compositions were studied on the parallelepiped-shaped samples with dimensions 5 mm × 5 mm × 20 mm and a relative density of 0.95.

The compositions studied in the work are presented in Table 1. The table shows these characteristics: density (ρ), adiabatic combustion temperature (T_{ad}). The ignition temperature (T_{ig}), combustion rate (V_c) of the initial samples and after MA are presented in Table 1.

Table 1. Compositions and their properties

No.	Compositions wt. %	ρ, g/cm³	T_{ad}, °C	T_{ig}, °C initial	T_{ig}, °C after MA	V_c, mm/s initial	V_c, mm/s after MA
1	65Hf–35PTFE–0Al	4.54	2381	680	650	0.3	4.0-4.5
2	62Hf–33PTFE–5Al	4.38	2642	680	570	1.1	4.5-5.5
3	58.5Hf–31.5PTFE–10Al	4.20	3327	660	590	2.0	4.0-4.5
4	55Hf–30PTFE–15Al	4.02	3368	690	630	4.5	3.5-4.0
5	52Hf–28PTFE–20Al	3.91	3127	620	620	3.0	4.5-5.0

The study was financially supported by the Russian Foundation for Basic Research within the framework of the scientific project No. 20-08-00640-A

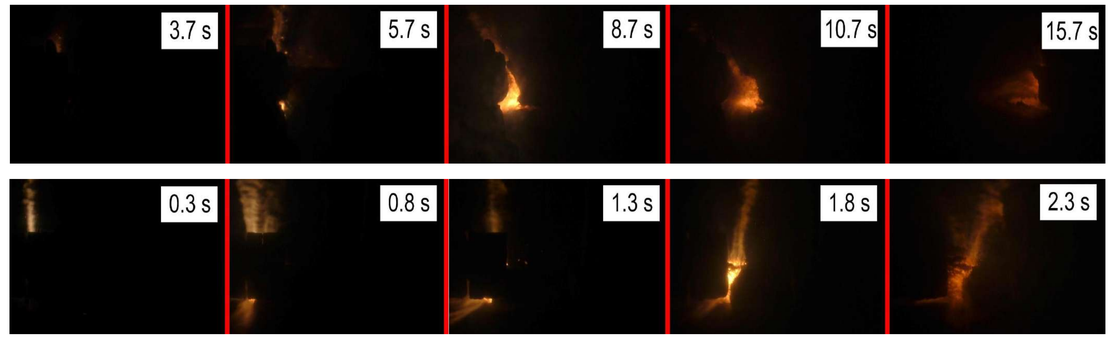

Figure 1. Video frames of combustion 5% Al (a) initial, (b) after MA

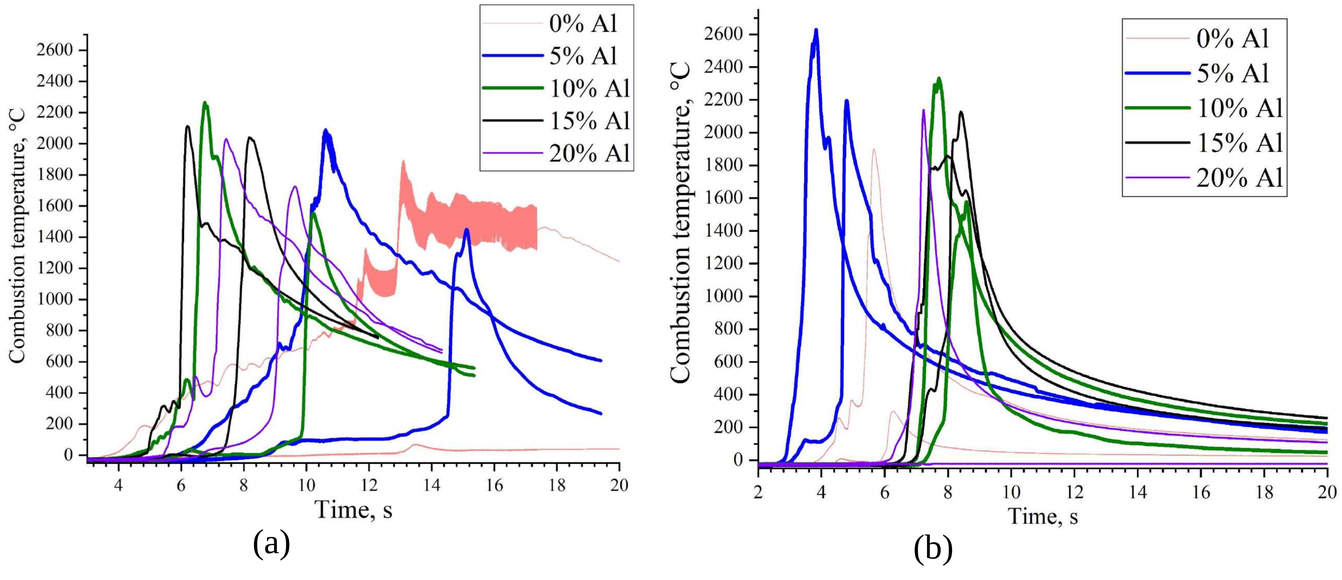

Figure 2. Thermograms of the combustion rate (a) initial, (b) after MA

It has been established that as a result of mechanical activation, the reactivity of the compositions increases. As evidenced by a decrease in the ignition temperature from 680 to 570 °C, an increase in the combustion rate from 1.1 to 5.5 mm/s and temperature from 2100 to 2650 °C in composition 5% Al. Mechanical activation improves the efficiency of the energy material due to the complete combustion of the components

SIALON-BESED HETERO-MODULUS CERAMIC COMPOSITES BY CS AND SPS

Smirnov K.L. ISMAN, kosm@ism.ac.ru

Introduction

Experimentally investigated was the R&D of hetero-modulus ceramic composites (HMCCs) SiAlON–BN HMCCs that recognized as promising multifunctional materials for high-temperature applications. Two schemes based on combustion synthesis (CS) and spark plasma sintering (SPS) were used: - direct infiltration-assisted CS in one stage under high-pressure nitrogen gas; - SPS of CSed raw powders.

Experimental

Direct infiltration-assisted CS of SiAlON–BN HMCCs was carried out under high pressure of nitrogen gas up to 150 MPa according to the following reaction scheme :

$3.45Si + 1.7Al + 0.85SiO_2 + N_2 \rightarrow \beta\text{-}Si_{4.3}Al_{1.7}O_{1.7}N_{6.3}$ (1)

$B + 0.5\ N_2 \rightarrow BN$ (2)

The some amount of $\beta\text{-}Si_{4.3}Al_{1.7}O_{1.7}N_{6.3}$ were added to starting reactive mixture as diluent to prevent high-temperature dissociation of end product and to suppress coagulation of low-melting combustible components. Starting mixtures were intermixed in a laboratory ball mill for 2 h, cold isostatic pressed (50 MPa) into cylindrical pellets with a relative density of 0.62–0.64, placed in a graphite crucible and then installed in a 4-L reaction chamber equipped with hydraulic gaseous compressor. The combustion reaction was ignited with an electrically heated tungsten coil.

Infiltration-assisted CS of raw powders for SPS was carried out by the following schemes:

$4.5Si + Al + 0.5SiO_2 + 3.5N_2 \rightarrow \beta\text{-}Si_5AlON_7$ (1)

$B + 0.5N_2 \rightarrow$ h-BN (2).

Starting mixtures also contained some amount of homemade diluents, $\beta\text{-}Si_5AlON_7$ and h-BN respectively, in order to improve extent of conversion. CS was performed in a 8-L reactor at $P(N_2)$ = 2–10 MPa. Aliquot amounts of CSed raw powders were intermixed in a high-energy planetary steel-ball mill. Milling time (800 rpm, ball/mill ratio 10:1) was 10 min. Then milled powders were sintered in a Labox 635 SPS facility under vacuum (~ 10 Pa). The heating rate was 50 °C/min. The sintered compacts were heated from room temperature to 600°C without applied load and then to 1500–1800°C at a compressive stress of 50 MPa. The compacts were held at a desired temperature for 5 min before the power was turned off.

Results and Discussion

With increasing nitrogen pressure the combustion parameters (temperature T_c and velocity U_c) gradually rise and then level off around 100 MPa (Fig. 1). Simultaneously, infiltration-assisted combustion transforms from surface to frontal mode. Direct infiltration-assisted CS is accompanied by sample shrinkage that also attains maximum (15-25 vol %) at $P(N_2)$=100 MPa. Thus obtained CSed HMCCs have relative density in the range of 0,75-0,88 and homogeneous microstructure with domination of fine irregularly shaped grains. Coarse regularly shaped grains with a typical morphology (flake-like h-BN and rod-like $\beta\text{-}Si_{4.3}Al_{1.7}O_{1.7}N_{6.3}$) appear only in large pores. The strength of HMCCs as a function of porosity (P) is in good agreement with the well-known expression $\sigma = \sigma_0 \exp(-4P)$, where σ_0 is 240–300 MPa and 400–550 MPa for bending and compression strength respectively. The strength characteristics of HMCCs is stable up to 1550 ^{0}C then drops down to 80–90 MPa. At the same time, CSed HMCCs are a pronounced high-temperature insulator, since their specific resistivity in this temperature range is 10^{12}-10^{13} Ω·cm. The CSed HMCCs exhibit high thermal-shock resistance typical of HMCCs obtained by HP: under quenching in water, they are capable of withstanding a 550–600°C temperature drop without any loss in strength. The CSed HMCCs also exhibit extremely high corrosion resistance to metallurgical melts. In this respect, they are much better than their analogs fabricated by conventional methods and commercially available refractories. Their corrosion stability is closely related to oxidation stability: negligibly low surface oxidation was only observed above 1400°C. Finally CSed HMCCs have excellent machinability. Some items (crucibles, nozzles for metal pouring, and lining plates) obtained by confentional hard alloy cutting tools are shown in Fig. 2.

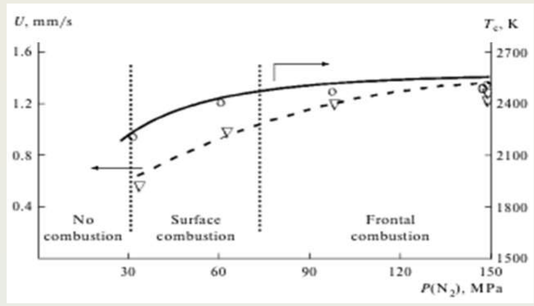

Fig. 1. Combustion temperature T_c and burning velocity U vs. nitrogen pressure.

Fig. 2. Items made of CSed HMCCs: crucibles, nozzles for metal pouring and lining plates.

Two type of $\beta\text{-}Si_5AlON_7$ raw powders (fine d_{av} = 0.6–1.0 μm and coarse d_{av} = 3.5–4.0 μm) were used for SPS of HMCCs. For all pure raw powders, the densification intensified markedly at T > 1400°C. That just corresponded formation of the liquid eutectics in SiO_2–Al_2O_3 surface oxides. The most intensive densification was registered for fine pure $\beta\text{-}Si_5AlON_7$ when high-density homogenous structure was already achieved at T_{max} = 1550°C. The relative density of coarse $\beta\text{-}Si_5AlON_7$ sintered at same condition was about 0.75–0.77, the their particles remained practically unchanged and only the formation of bottle necks in contact points. With further increase in T_{max} the relative density gradually grows up to 0.87. According to XRD data, coarse pure $\beta\text{-}Si_5AlON_7$ sintered above 1750°C exhibits the traces of AlN formed upon thermal decomposition. The addition of h-BN facilitates densification by improving the compatibility of powder mixtures. Under a compressive stress of 50 MPa at 600°C, the relative density of compacts containing 30 wt % h-BN exceeds 0.80 for types of raw powders. As a result, SPSed HMCCs attain high-density structure already at T_{max} = 1550°C for all types of $\beta\text{-}Si_5AlON_7$ raw powders. Meanwhile fine grained HMCCs have homogenous distribution of flake-like h-BN particles among $\beta\text{-}Si_5AlON_7$ matrix while in coarse grained HMCCs flake-like h-BN particles have tendency to form shells around $\beta\text{-}Si_5AlON_7$ large grains (Fig. 3). SPSed coarse grained HMCCs (5-30 wt % h-BN) have bending strength in the range of 250–300 MPa while bending strength of fine grained is significantly higher (400–500 MPa).

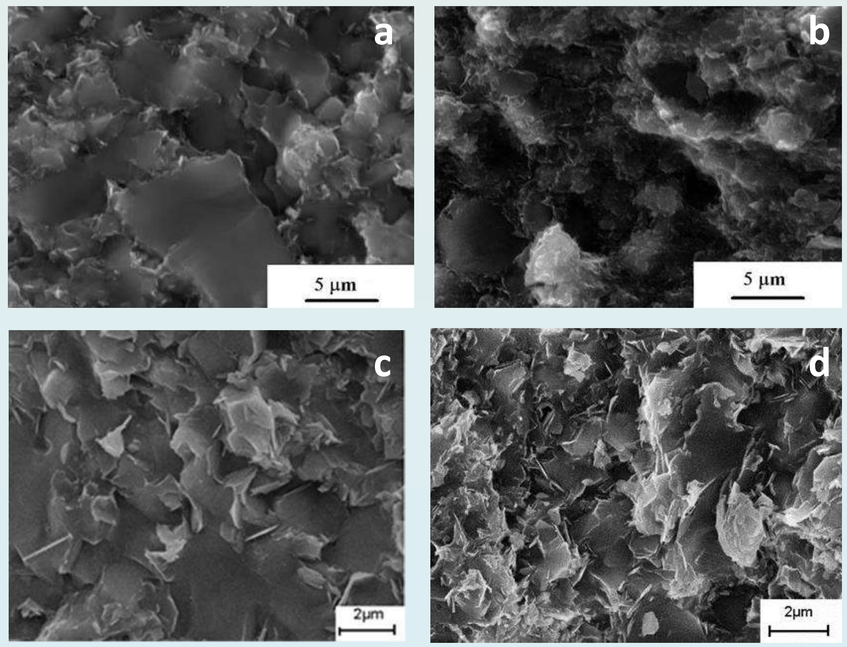

Fig. 3. Fracture surface of coarse grained (a, b) and fine grained (c, d) HMCCs containing h-BN: 10 wt. % (a, c) and 30 wt. % (b, d).

IV International Conference and School "Advanced High Entropy Materials"
September 26-30, 2022

№ 56

buynevich.vs@misis.ru

FABRICATION OF NOVEL REFRACTORY CARBONITRIDE CERAMICS FOR HIGH-TEMPERATURE APPLICATIONS BY COMBUSTION SYNTHESIS AND SPARK PLASMA SINTERING

V.S. Suvorova (Buinevich), A.A. Nepapushev, K.V. Kuskov, D.O. Moskovskikh

RELEVANCE

According to modeling, under the influence of powerful heat flows (2-6 MW/m^2), structural units and hull elements of progressive aircraft are subjected to local convective heating up to temperatures of about 2500 °C (Fig. 1) [1].

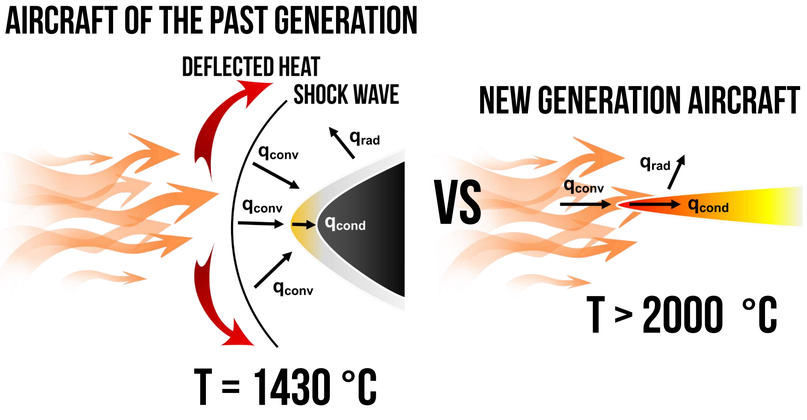

Fig. 1 Temperature distribution over the wing surface of an aircraft of the past and new generation

AIM OF WORK

Obtaining refractory ceramics (Ta,Hf)CN and Hf(C,N) by energy-efficient methods of combustion synthesis (CS) and spark plasma sintering (SPS), study of their mechanical, thermophysical properties and oxidation resistance.

METHODS

Refractory ceramics are obtained by a combination of mechanical activation, combustion synthesis and spark plasma sintering methods (Fig. 2).

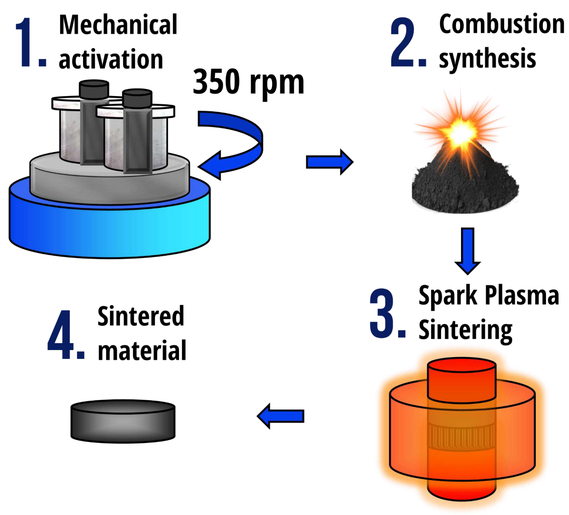

Fig. 2 Scheme for obtaining refractory ceramics

RESULTS

In this work, UHTCs based on hafnium carbonitride Hf (C, N) and (Ta, Hf) CN were obtained by CS and SPS with a relative density above 98 % and a hardness of 21.3 and 19.4 GPa, respectively. The incorporation of nitrogen atoms into the HfC lattice contributed to an increase in the melting point from 4200 [2] to 4300 °C (Fig. 3), thermal conductivity by 75 %, and oxidation resistance by 40 %.

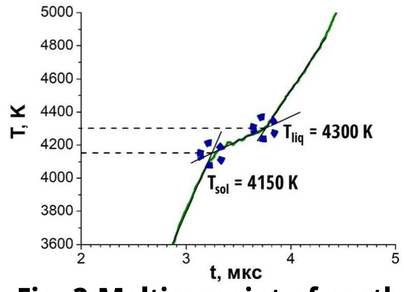

$T_{пл}$ (HfC) = 4200 ± 80 K [3]

$T_{пл}$ ($Ta_{0,8}Hf_{0,2}C$) = 4300 ± 80 K [4]

$T_{пл}$ ($HfC_{0,5}N_{0,35}$) = 4300 ± 80 K

Fig. 3 Melting point of synthesized Hf(C,N)

Tantalum-hafnium carbonitride with a high hafnium content demonstrated higher oxidation resistance in a high-temperature gas flow (mass oxidation rate - 0.15 mg/s; linear oxidation rate - 0.8 μm/s) compared to tantalum hafnium carbide (0.67 mg/s, 2.38 μm/s) [3].

BIBLIOGRAPHY

1. Monteverde F., Savino R. ZrB2–SiC sharp leading edges in high enthalpy supersonic flows //Journal of the American Ceramic Society. – 2012. – Т. 95. – №. 7. – С. 2282-2289.
2. A.I. Savvatimskiy, S. V. Onufriev, S.A. Muboyadzhyan, Thermophysical properties of the most refractory carbide Ta0.8Hf0.2C under high temperatures (2000–5000 K), J. Eur. Ceram. Soc. (2019).
3. Zhang J. et al. Ultra-high temperature ablation property of Ta0. 5Hf0. 5C ternary ceramic under plasma flame //Ceramics International. – 2021. – Т. 47. – №. 19. – С. 28050-28054.

IV International Conference and School "Advanced High Entropy Materials"
September 26-30, 2022

№59

1249552@bsu.edu.ru

INVESTIGATION OF THE EFFECT OF ALUMINUM ON THE STRUCTURE AND MECHANICAL PROPERTIES OF MEDIUM ENTROPY ALLOYS $Al_xNb_{40}Ti_{40}V_{20-x}$

Tojibaev A. A., Panina E. S., Zhilina M. A., Klimenko D. N., Yurchenko N. Yu.

Laboratory of Bulk Nanostructured Materials, Belgorod State University, 85 Pobeda Str., 308015, Belgorod, Russian Federation.

Abstract

High/medium-entropy alloys based on refractory elements (RH/MEAs) represent a new class of alloys with promising high-temperature properties. Currently, the influence of individual elements on the structure and mechanical properties of RH/MEAs is being studied actively. For example, the addition of Al was shown to result in the formation of a B2 ordered structure. Many RH/MEAs with the B2 structure demonstrate high strength but extremely low ductility, even under compression tests. One of the ways to achieve more balanced properties is the variation of the chemical composition. Specifically, previous works reported that reducing the Al content or adding of Zr to some RH/MEAs increased compressive ductility by lowering the degree of B2 ordering. In this work, we studied the effect of Al on the structure and mechanical properties of $Al_xNb_{40}Ti_{40}V_{20-x}$ (x = 0; 5; 10; 15; 20 at.%) RMEAs.

Microstructure

Alloy ingots were obtained by vacuum-arc melting of high-purity (> 99.9 wt.%) elements in argon in a water-cooled copper mold. The ingots were rolled to a degree of deformation of 80% and annealed in a quartz tube with a vacuum of 10^{-2} torr and kept in a «Nabertherm» furnace at temperatures T=1200°C with a holding time of 5 minutes for the $Nb_{40}Ti_{40}V_{20}$ alloy, T=1000°C for 1 hour for $Al_5Nb_{40}Ti_{40}V_{15}$ alloy, T=1000°C 30 minutes for $Al_{10}Nb_{40}Ti_{40}V_{10}$ alloy, T=1050°C 15 min for $Al_{15}Nb_{40}Ti_{40}V_5$ alloy and T=1200°C 1 min for $Al_{20}Nb_{40}Ti_{40}$ alloy followed by water quenching. The annealing regime was chosen in such a way as to establish the size correspondence of the alloy grains. The microstructure of the alloys was studied using SEM and TEM methods.

EBSD analysis showed that the microstructure of the alloys consisted of a single-phase BCC structure with polygonal recrystallized grains. The average grain size was ~30 μm.

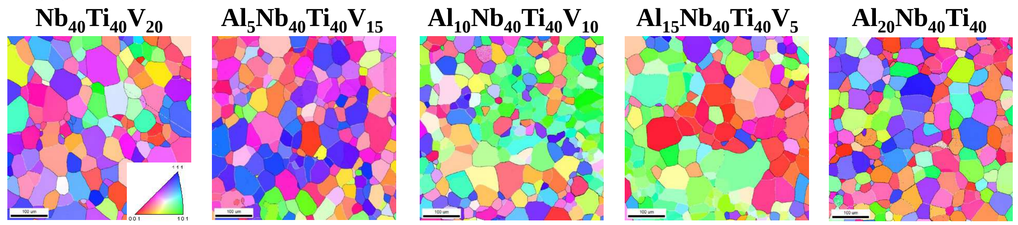

$d_{av} = 36 \pm 20$ μm $d_{av} = 30 \pm 17$ μm $d_{av} = 28 \pm 14$ μm $d_{av} = 31 \pm 20$ μm $d_{av} = 31 \pm 17$ μm

For a more detailed analysis of the phase composition of the alloys, TEM was used. In the $Nb_{40}Ti_{40}V_{20}$ and $Al_5Nb_{40}Ti_{40}V_{15}$ alloys, there were no {100} superlattice reflections, which indicated the formation of a bcc structure. In the $Al_{10}Nb_{40}Ti_{40}V_{10}$, $Al_{15}Nb_{40}Ti_{40}V_5$, and $Al_{20}Nb_{40}Ti_{40}$alloys, superlattice reflections {100} were found, the intensity of which, according to the profile analysis of electron diffraction patterns (along $\vec{g}$ = 200), increased from the $Al_{10}Nb_{40}Ti_{40}V_{10}$ alloy to the $Al_{20}Nb_{40}Ti_{40}$ alloy, which indicated a B2 structure and an increase in the degree of B2 ordering.

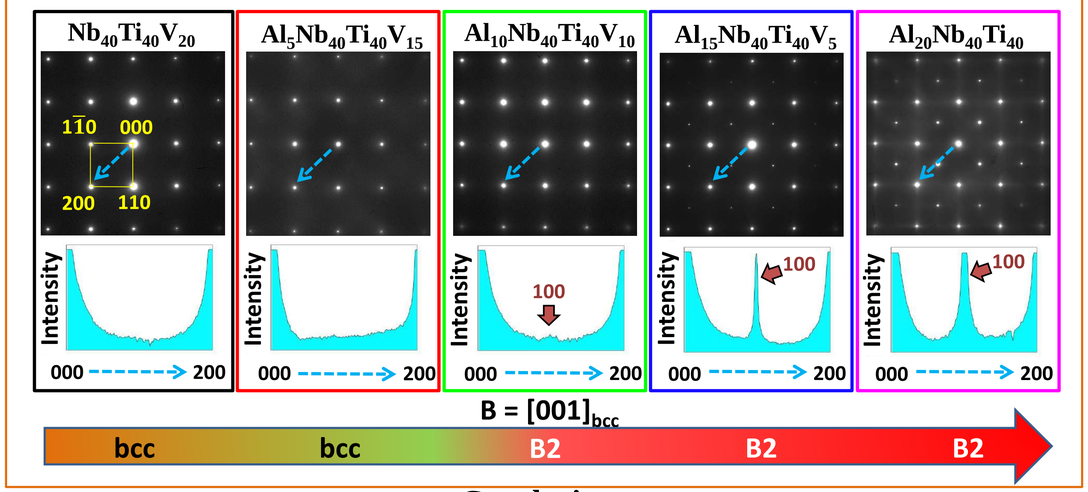

Conclusions

1. The structure of alloys of the $Al_xNb_{40}Ti_{40}V_{20-x}$ system has been studied. According to the EBSD analysis, a single-phase bcc structure was formed in all alloys. However, a more detailed study using transmission electron microscopy revealed the formation of a B2 ordered structure in the $Al_{10}Nb_{40}Ti_{40}V_{10}$, $Al_{15}Nb_{40}Ti_{40}V_5$, and $Al_{20}Nb_{40}Ti_{40}$ alloys.
2. Mechanical properties of alloys of the $Al_xNb_{40}Ti_{40}V_{20-x}$ system were analyzed during tensile tests at room and elevated temperatures. The results show a complex relationship between mechanical properties and the aluminum content of the alloys. With the addition of aluminum up to 15 at.%, room-temperature ductility increases, while the $Al_{20}Nb_{40}Ti_{40}$ alloy was brittle. The temperature rise softened and ductilized all the alloys.

Mechanical Properties

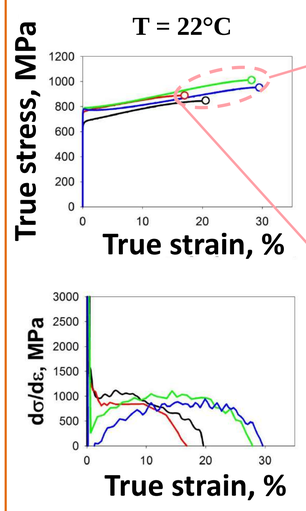

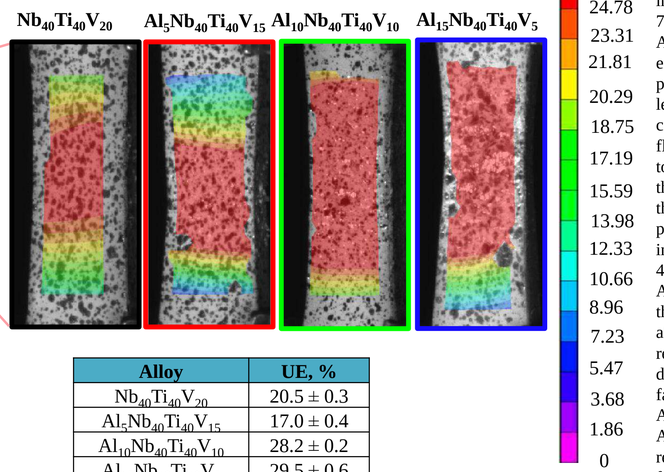

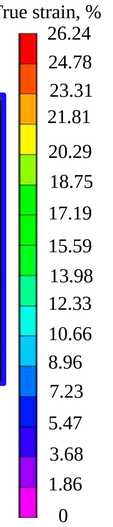

Alloy	UE, %
$Nb_{40}Ti_{40}V_{20}$	20.5 ± 0.3
$Al_5Nb_{40}Ti_{40}V_{15}$	17.0 ± 0.4
$Al_{10}Nb_{40}Ti_{40}V_{10}$	28.2 ± 0.2
$Al_{15}Nb_{40}Ti_{40}V_5$	29.5 ± 0.6
$Al_{20}Nb_{40}Ti_{40}$	-

Room temperature tests were recorded with high speed digital image correlation (DIC) cameras using VIC-3D software. With the addition of aluminum, an increase in the ultimate strength was observed from 710 MPa in the $Nb_{40}Ti_{40}V_{20}$ alloy to 770 MPa in the $Al_{10}Nb_{40}Ti_{40}V_{10}$ alloy. Meanwhile, the analysis of engineering stress – engineering curves showed the presence of a yield drop and plateau, the size and length of which increased with an increase in the Al content, which could indicate the instability of plastic flow. However, the true stress-true strain curves, together with DIC analysis of the working parts of the test specimens, showed that the addition of Al, on the contrary, contributed to the delocalization of plastic deformation. Thus, the uniform elongation increased from 37.5% in the $Nb_{40}Ti_{40}V_{20}$ alloy to 42.2% in the $Al_{15}Nb_{40}Ti_{40}V_5$ alloy.

According to the plot of the dependence of strain on the strain hardening rate in the $Nb_{40}Ti_{40}V_{20}$ alloy, after the yield point, where the strain hardening rate reaches its maximum values, there is a sharp decrease to 1000 MPa and a uniform decrease until failure. A similar picture is also observed in the $Al_5Nb_{40}Ti_{40}V_{15}$ alloy. In $Al_{10}Nb_{40}Ti_{40}V_{10}$ and $Al_{15}Nb_{40}Ti_{40}V_5$ alloys, after a sharp decrease, respectively, a recovery in the strain hardening rate followed by a steady state was observed with the strain increment.

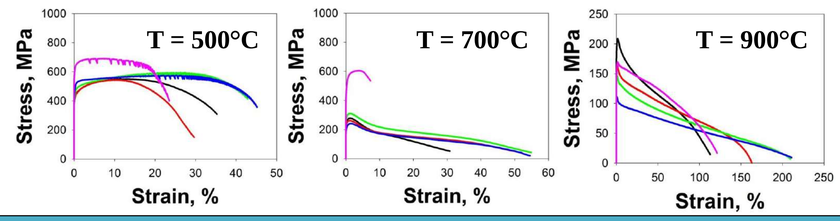

Alloy	Testing temperature, °C											
	22			500			700			900		
	YS*, MPa	UTS, MPa	EF,%	YS, MPa	UTS, MPa	EF,%	YS, MPa	UTS, MPa	EF,%	YS, MPa	UTS, MPa	EF,%
$Nb_{40}Ti_{40}V_{20}$	660	710	37.5	420	550	35.3	245	275	30.8	180	210	113.0
$Al_5Nb_{40}Ti_{40}V_{15}$	750	770	35.5	415	545	29.6	240	260	52.1	140	165	163.8
$Al_{10}Nb_{40}Ti_{40}V_{10}$	770	785	45.9	440	595	42.9	285	310	54.9	135	145	209.6
$Al_{15}Nb_{40}Ti_{40}V_5$	750	775	45.6	480	575	45.1	210	240	54.6	105	110	211.1
$Al_{20}Nb_{40}Ti_{40}$	795	800	0.3	620	690	23.5	510	605	7.1	150	170	121.2

***YS – Yield strength; UTS – Ultimate tensile strength; EF – elongation to fracture**

The results obtained after testing specimens for uniaxial tension at temperatures of 500, 700, and 900°C and a strain rate of 10^{-3} s^{-1} showed a complex relationship between mechanical properties and aluminum content in the composition of alloys. The $Al_{20}Nb_{40}Ti_{40}$ alloy demonstrated the highest yield strength of 620 MPa at 500°C and 510 MPa at 700°C (twice higher than those of the $Nb_{40}Ti_{40}V_{20}$ and $Al_5Nb_{40}Ti_{40}V_{15}$ alloys). At 900°C, the $Nb_{40}Ti_{40}V_{20}$ was the strongest, while the $Al_{10}Nb_{40}Ti_{40}V_{10}$ and $Al_{15}Nb_{40}Ti_{40}V_5$ possessed the highest ductility.

Acknowledgements

The authors gratefully acknowledge the financial support from the Russian Science Foundation Grant no. 21-79-10043 (https://rscf.ru/en/project/21-79-10043/). The work was carried out using the equipment of the Joint Research Center of Belgorod State National Research University «Technology and Materials» with financial support from the Ministry of Science and Higher Education of the Russian Federation within the framework of agreement № 075-15-2021-690 (unique identifier for the project RF----2296.61321X0030).